# Statistical distribution of mirror mode-like structures in the magnetosheaths of unmagnetised planets: 1. Mars as observed by the MAVEN spacecraft

Cyril Simon Wedlund[1], Martin Volwerk[1], Christian Mazelle[2], Sebastián Rojas Mata[3], Gabriella Stenberg Wieser[3], Yoshifumi Futaana[3], Jasper Halekas[4], Diana Rojas-Castillo[5], César Bertucci[6], and Jared Espley[7]

[1]Austrian Academy of Sciences, Space Research Institute, Graz, Austria
[2]Institut de Recherche en Astrophysique et Planétologie (IRAP), Université de Toulouse, CNRS, UPS, CNES, Toulouse, France
[3]Swedish Institute of Space Physics, Kiruna, Sweden
[4]Department of Physics and Astronomy, University of Iowa, Iowa City, IA, USA
[5]Instituto de Geofísica, Universidad Nacional Autónoma de México, Coyoacán, Mexico
[6]Instituto de Astronomía y Física del Espacio, Ciudad Autónoma de Buenos Aires, Argentina
[7]NASA Goddard Space Flight Center, Laboratory for Planetary Magnetospheres, Greenbelt, MD, USA

**Correspondence:** Cyril Simon Wedlund (cyril.simon-wedlund@oeaw.ac.at)

**Abstract.** In this series of papers, we present statistical maps of mirror mode-like (MM) structures in the magnetosheaths of Mars and Venus and calculate the probability of detecting them in spacecraft data. We aim to study and compare them with the same tools and a similar payload at both planets. We consider their dependence on Extreme Ultraviolet (EUV) solar flux levels (high and low), and, specific to Mars, on Mars Year (MY) as well as atmospheric seasons (four solar longitudes Ls).

5   We first use magnetic field-only criteria to detect these structures and present ways to mitigate ambiguities in the nature of the detected structures. In line with many previous studies at Earth, this technique has the advantage of using one instrument (a magnetometer) with good time resolution facilitating comparisons between planetary and cometary environments. Applied to the magnetometer data of the Mars Atmosphere and Volatile EvolutioN (MAVEN) spacecraft from November 2014 to February 2020 (MY32–MY35), we detect structures closely resembling MMs lasting in total more than $170,000\,\mathrm{s}$, corresponding to

10   about 0.1% of MAVEN's total time spent in the Martian plasma environment. We calculate MM-like occurrences normalised to the spacecraft's residence time during the course of the mission. Detection probabilities are about 1% at most for any given controlling parameter. In general, MM-like structures appear in two main regions, one behind the shock, the other close to the induced magnetospheric boundary, as expected from theory. Detection probabilities are higher on average in low solar EUV conditions, whereas high solar EUV conditions see an increase in detections within the magnetospheric tail. We tentatively

15   link the former tendency to two combining effects: the favouring of ion cyclotron waves the closer to perihelion due to plasma beta effects, and, possibly, the nongyrotropy of pickup ion distributions. This study is the first of two on the magnetosheaths of Mars and Venus.

# 1 Introduction

Mirror modes (MMs) are magnetic bottles of various sizes and shapes containing high-density plasma drifting with the ambient
20   plasma. They are often found in the magnetosheaths of solar system objects, some magnetised like Earth (e.g., Lucek et al.,
1999; Ala-Lahti et al., 2018, and references therein), others non magnetised or weakly magnetised like comets (Mazelle et al.,
1991; Glassmeier et al., 1993), Venus (see Volwerk et al., 2016, and references therein) and Mars (see Simon Wedlund et al.,
2022c, and references therein).

Arising from plasma microinstabilities themselves triggered by an ion temperature anisotropy in the plasma, MM waves are
25   compressional, essentially linearly polarised, ultra low-frequency, long-wavelength transverse waves which are non-propagating
in the plasma rest frame (Gary, 1992). The drift MM instability is typically triggered in a weakly magnetised plasma (that is,
in a high plasma beta $\beta \gg 1$), a condition that is met in a planetary magnetosheath, whereas the Alfvén ion cyclotron instability
takes over for low plasma-$\beta$ conditions. The MM instability is expected to grow when the MM instability criterion (MMI) is
fulfilled (Hasegawa, 1969):

$$\text{MMI} = 1 + \sum_i \beta_{i\perp} \left(1 - \frac{T_{i\perp}}{T_{i\parallel}}\right) < 0, \tag{1}$$

where subscripts $\parallel$ and $\perp$ denote the directions parallel and perpendicular to the ambient magnetic field direction $\mathbf{B}_{\text{bg}}$. The
ion temperature is noted $T_i$, and the perpendicular plasma beta $\beta_{i\perp}$ measures the competing effects of plasma and magnetic
pressures so that $\beta_{i\perp} = 2\mu_0 N_i k_B T_{i\perp}/|B|^2$, with $N_i$ the ion density.

Several mechanisms at the origin of the temperature anisotropy have been proposed (Gary, 1993). At every object with
35   a well-defined bow shock (Earth, Mars, Venus and comets nearing perihelion), the quasi-perpendicular shock provides in
its wake a preferential heating of the ions along the perpendicular direction to the magnetic field, favouring the generation
of MMs. Another possibility exists, specific to environments with weak gravity (Mars, Venus, comets): in their extended
exosphere, ions created by photoionisation are picked up by the solar wind (Szegö et al., 2000). In the plasma rest frame, the
velocity distribution function of these pickup ions takes the form of an unstable ring-beam distribution, with the relative value
40   of both parallel and perpendicular components depending only on the local cone angle between the $\mathbf{B}$-field and the bulk plasma
velocity vector at the location of the ionisation. For large-enough cone angles, the ring component of the distribution results in
an ion temperature anisotropy $T_\perp/T_\parallel > 1$, which is a source of free energy for microinstabilities such as MMs (Price, 1989).

Because of their stationary nature, MMs can be convected downstream of their birth place, likely unchanged, by their
surrounding plasma. As a consequence, many structures end up piling up against the magnetospheric boundary in the deep
45   magnetosheath, where they are finally detected, as for example shown by Earth observations close to the magnetopause (Erkaev
et al., 2001).

In spacecraft data, the signature of MMs takes the form of sudden dips or peaks in the magnetic field intensity in antiphase
with plasma density variations, lasting a few seconds to tens of seconds. Considering that spacecraft are essentially at rest with
respect to the ambient plasma and for plasma speeds of the order of 100 km/s, their sizes are at Mars of the order of a not
50   insignificant fraction of a planetary radius $R_M$=3389.5 km. In addition, MMs likely share a common ancestor with magnetic

holes (MHs), which are isolated magnetic field depressions usually found in the upstream solar wind (e.g., Volwerk et al., 2021; Madanian et al., 2020, and references therein) or in the magnetosheath of planets (e.g., Karlsson et al., 2021).

Traditionally, several ways of detecting MM structures have been used. The most widespread and easiest method is to use magnetic field-only measurements with ad-hoc criteria constraining the compressibility and the quasi-linear polarisation of the

55 detected structures (Soucek et al., 2008; Génot et al., 2009). It has the advantage of using a well-calibrated instrument, the magnetometer, that has been flown on many space missions and has a high temporal resolution, good accuracy and excellent reliability over an extended mission lifetime. However, ambiguities in the nature of the detected structures always remain: for example highly compressional structures may meet all $B$-field criteria without necessarily fulfilling the MMI or the $B$–$N$ anticorrelation behaviour, pointing to other types of waves (Song et al., 1994). Moreover, the criteria chosen are somewhat

60 arbitrary and may either include many false positive detections or miss altogether most of the events if too stringent. Most of these ambiguities can at least be partially lifted with the use of dedicated plasma measurements (Gary and Winske, 1992).

A complementary approach is to use the property of MMs of having variations in $B$ and plasma density $N_p$ in antiphase. One caveat is that plasma measurements need to have sufficient temporal resolution to be able to capture structures not lasting more than a few tens of seconds: many ion instruments on earlier planetary space missions such as Mars Express or Venus

65 Express (VEX) have a 192-s scanning rate, which is much too low to be of help. Electron measurements can fare better: at Mars for example, Bertucci et al. (2004) looked instead at the $B$–$N_e$ antiphase behaviour ($N_e$ being the electron density) of highly compressional linear structures to argue in favour of MMs. This was also because no ion instrument was flown on Mars Global Surveyor (MGS).

A separate approach using plasma measurements and magnetic field data relies on the hierarchical scheme of Gary and

70 Winske (1992); Song et al. (1994) based on so-called 'transport' ratios that formalise correlations in Fourier space between magnetic field and plasma pressure. This method is well suited for statistical surveys and has successfully been used at Mars by Ruhunusiri et al. (2015) and at Venus by Fränz et al. (2017). Both studies presented two-dimensional maps of the distribution of low-frequency wave modes, showing that MMs are present in the magnetosheath and magnetotail at probabilities of less than 20%, whereas the bulk of the wave activity is contained in the Alfvén and quasi-parallel slow modes. This method is

75 dependent on the plasma measurements and their Fourier analysis, which makes use of rather large temporal windows to be computationally feasible. Moreover, it is based on magnetohydrodynamic considerations, which may not be entirely reliable for kinetic microinstabilities (Schwartz et al., 1997).

Alternatively, and to lift most ambiguities, the precise study of the MMI, with the derivation of robust ion and electron temperature anisotropy estimates at enough time resolution to be relevant to MMs, is ideally the best way of characterising

80 MMs. This remains however to this day a challenging task more suited to case studies. Such an in-depth characterisation of MMs was for the first time made by Simon Wedlund et al. (2022c). It was made possible by the arrival in 2014 at Mars of the Mars Atmosphere and Volatile EvolutioN (MAVEN) spacecraft, which carries magnetometer (Connerney et al., 2015) and high-time resolution plasma instruments, such as the Solar Wind Ion Analyzer (SWIA, Halekas et al., 2015) and the Solar Wind Electron Analyzer (SWEA Mitchell et al., 2016). Simon Wedlund et al. (2022c) described a classical event in December

85 2014 at the end of Mars Year 32 (MY32) containing a train of MMs lodged against the Induced Magnetospheric Boundary

(IMB). From considerations on the MMI and the size of these structures, the authors argued for a remote generation region in the immediate wake of the quasi-perpendicular bow shock, in a way similar to Earth observations (see Erkaev et al., 2001). With MAVEN, Halekas et al. (2017a) presented for the first time maps of the distribution of the temperature anisotropy at Mars using the maximum temperature perpendicular to the ambient magnetic field. Predictably, the Martian magnetosheath

90  exhibits a strong anisotropy especially at regions controlled by the quasi-perpendicular shock for low Mach numbers. These anisotropies are especially conducive to the growth of MMs and Alfvén ion cyclotron waves.

We aim in this series of papers to provide for the first time occurrence probability maps in different conditions at Mars (present paper, abbreviated Paper I) and Venus (Paper II, Volwerk et al., 2022) using the same method of investigation. For simplicity, reproducibility and to allow future comparisons at other solar system objects such as comets, we opt for a magnetic

95  field-only analysis in the same way as Volwerk et al. (2008, 2016) using the magnetometers on board MAVEN and VEX. Contrary to Venus, no long-term statistical study has ever been dedicated to MMs at Mars, a lack we propose to address here. In this way, we have the unique chance of directly comparing planets with the very same detection criteria, here based for example on the recommendations of Simon Wedlund et al. (2022c). Although ambiguities do remain regarding the nature of the detected structures, such a comparison remains meaningful as long as we are careful to remove 'false positive' candidate

100  structures that are obviously not MMs. Such a work will serve as basis for reevaluating past datasets at Mars, Venus and comets.

In Section 2, we present our method of detection of MM-like events at Mars, based on **B**-field only criteria determined statistically from a subset of carefully chosen data. After describing techniques to mitigate the presence of false positive detections (Section 2.2.2), we apply the **B**-field only criteria to the whole MAVEN magnetometer dataset between Nov. 2014 and Feb. 2021, covering four Mars Years, MY32 to MY35 included (Section 2.2.3). We proceed to create 2-D maps of MM-like

105  events normalised by the spacecraft residence time, which are in effect a probability to observe MM-like structures within a given grid cell (Section 2.3). We then study and discuss in Section 3 the dependence of these probabilities on several physical parameters of interest, such as Mars Year (MY), solar EUV flux and Mars season, parametrised by the solar longitude Ls. For simplicity in this first comparative study based on a magnetic field single perspective, solar wind drivers such as dynamic pressure, interplanetary magnetic field configuration and strength or the nature of the shock, are left for a future work. We

110  conclude our present study with suggestions for improvements and new controlling parameters to explore (Section 4).

## 2  Detecting mirror mode-like structures

### 2.1  Instrumentation

We use for this study the magnetic field investigation package onboard MAVEN (abbreviated MAG in the following), which consists of two tri-axial fluxgate magnetometers mounted at the extremity of boomlets on the spacecraft's solar panels (Con-

115  nerney et al., 2015). It allows the measurement of the 3 components of the magnetic field with a nominal frequency of 32 Hz and an accuracy better than 0.05%. Because the structures we are looking for in the dataset are expected to last from a few seconds up to 15–20 s (Simon Wedlund et al., 2022c), the high-time resolution of the instrument is downsampled to 1 s.

As supporting instrument for the event cases shown in Figs. 1 and 2 (last panel), we use MAVEN's Solar Wind Ion Analyzer (SWIA) electrostatic ion analyser, which measures ion differential fluxes with a maximum temporal resolution of 4 s (Halekas et al., 2015). Specific modes are available depending on energy/angle scanning and telemetry modes; we considered two modes here, SWICA (SWIA Coarse Archive, 8-s resolution), suited to magnetosheath conditions, and SWIFA (SWIA Fine Archive, 4-s resolution), designed for the monitoring of solar wind ions. Density moments are manually calculated from SWICA and SWIFA modes depending on the region considered.

## 2.2 Detection method

The detection of MM-like structures is based on spacecraft magnetometer data using magnetic field-only criteria. This has the advantage of a faster and unified detection across planets such as Mars or Venus, at the expense of the certainty that these detections are MM proper. We follow here the recommendations of Simon Wedlund et al. (2022c). These authors first used magnetic field and plasma data in coincidence to identify the unmistakable signature of a train of MMs during the early part of the mission and could then validate a set of $B$-field-only criteria to closely match these observations. Their rearranged series of criteria are listed in Table 1 for convenience. These criteria assume that the sought structures are compressional in nature (Criterion 1) and that they are quasi-linearly polarised (Criteria 2–4). Criteria 1–4 need to be simultaneously fulfilled in order for a MM-like structure to be selected. After the initial detection, additional constraints can be put on the found intervals such as Criterion 5 (quasi-linear polarisation) and Criterion 6 (presence in the magnetosheath as opposed to in the solar wind). We briefly describe these criteria in Section 2.2.1, as the reader is referred to Simon Wedlund et al. (2022c) (and references therein) for further consideration and motivation regarding the specific values chosen for each criterion.

Because the method is based only on criteria on the magnetic field and not on a more involved plasma data analysis, the possibility of false positive detections exists: we describe steps to mitigate this aspect in Section 2.2.2, with caveats discussed in Section 2.2.3. Consequently, the structures we are expected to detect here are dubbed *mirror mode-like* in the following ('MM-like'), to use the original nomenclature of Volwerk et al. (2008) at Venus.

### 2.2.1 B-field only criteria

First, we estimate the background magnetic field intensity $B_{bg}$ using a low-pass Butterworth filter as in Volwerk et al. (2016) for Venus and Simon Wedlund et al. (2022c) for Mars. We adopt a 2-min window ($f_{band} = 1/120$ Hz), a passband ripple of 2 dB and a stopband attenuation of 20 dB.

Criterion 1 ensures that the absolute $B$-field fluctuation is:

$$\frac{\Delta|\mathbf{B}|}{B_{bg}} = \frac{\left||\mathbf{B}| - B_{bg}\right|}{B_{bg}} \geq 0.15, \tag{2}$$

that is, magnetic field fluctuations are larger or equal than 15% of the background field. To obtain criteria 2–4, we then perform a moving minimum variance analysis (noted MVA, see Sonnerup and Scheible, 1998) with a 15-s moving window, which is about the width of the larger MM structures found at Mars (Simon Wedlund et al., 2022c), and a shift of 1 s. From the MVA, we define two angles: $\Theta_{maxV}$ ($\Phi_{minV}$) is the angle between the maximum (minimum) variance eigenvector direction and

**Table 1.** Magnetic field-only criteria for detecting MM-like structures (adapted from Simon Wedlund et al., 2022c): magnetic field fluctuation $\Delta|\mathbf{B}|/B_{bg}$ (Criterion 1); MVA angles $\Theta_{maxV}$ ($\Phi_{minV}$) between maximum (minimum) variance direction and that of $\mathbf{B}_{bg}$ (Criterion 2); ratio of MVA eigenvalues $\lambda_{max}/\lambda_{int}$ ($\lambda_{int}/\lambda_{min}$) between maximum (intermediate) and intermediate (minimum) eigenvalues (Criteria 3 and 4); moving standard deviation of magnetic azimuth and elevation angles $\langle\sigma(az,el)\rangle$ (Criterion 5) and average background field over a 2-min interval (Criterion 6). We use most of the revised set of values in Simon Wedlund et al. (2022c), except for $\Delta|\mathbf{B}|/B_{bg} \geq 0.14$ changed to 0.15, $\Theta_{maxV}$ changed from $\leq 23°$ to $\leq 20°$ for symmetry. The angular variation across a train of structures is estimated by calculating the moving standard deviation noted $\langle\sigma(az,el)\rangle$ over a 2-min period (in accordance with the background field calculations; because angular variations in magnetic field azimuth and elevation need to be kept below $\lesssim 20°$ for linearly polarised structures, we choose here $\langle\sigma(az,el)\rangle \leq 10°$.

| # | Criterion | Value | Reason | Inspired from |
|---|-----------|-------|--------|---------------|
| 1 | $\Delta|\mathbf{B}|/B_{bg}$ | $\geq 0.15$ | Compressional structure | Génot et al. (2009); Volwerk et al. (2016) |
| 2 | $\Theta_{maxV}$ | $\leq 20°$ | Linearly polarised waves | Lucek et al. (1999); Volwerk et al. (2016) |
|   | $\Phi_{minV}$ | $\geq 70°$ | Linearly polarised waves | Lucek et al. (1999); Volwerk et al. (2016) |
| 3 | $\lambda_{max}/\lambda_{int}$ | $\geq 2.5$ | Linearly polarised waves | Génot et al. (2001); Soucek et al. (2008) |
| 4 | $\lambda_{int}/\lambda_{min}$ | $\leq 8$ | Linearly polarised waves | Génot et al. (2001); Soucek et al. (2008) |
| 5 | $\langle\sigma(az,el)\rangle$ | $\leq 10°$ | Linearly polarised waves | Treumann et al. (2004); Tsurutani et al. (2011) |
| 6 | $\langle B_{bg}\rangle$ | $\geq 2B_{imf}$ | Magnetosheath conditions | Dimmock et al. (2015) |

150 that of the background magnetic field. A small (large) enough angle denotes a structure that is quasi-linear in polarisation, as expected and shown in the kinetic MM simulations of Price et al. (1986). We use also the ratio of the maximum-to-intermediate eigenvalues $\lambda_{max}/\lambda_{int}$ (intermediate-to-minimum eigenvalues $\lambda_{int}/\lambda_{min}$) to further constrain the shape of the variance ellipsoid into a cigar-shaped one (Génot et al., 2001).

At this stage and using Criteria 1–4, the total number of detected 1-s duration MM-like events in the 1 Nov. 2014–7 Feb. 155 2021 MAVEN dataset was 2,046,533. Two examples of **B**-field-only detections are presented in Figs. 1 (higher solar activity conditions) and 2 (lower solar activity) as structures in green and grey. We will come back to discussing them in Sect. 2.2.3.

### 2.2.2 Removal of false positive detections

The detection method presented in Table 1 does not exclude structures which may resemble MMs but, in effect, are not. Such structures, appearing as highly compressional, can be generated in and around the bow shock surface and testify to the 160 variability and complex structure of the Martian shock. These non-MM structures include upstream waves (see Mazelle et al., 2004; Romanelli et al., 2013, 2016; Dubinin and Fraenz, 2016; Romeo et al., 2021; Jarvinen et al., 2022, for observations and simulations). However, in contrast to MMs, they are usually circularly or elliptically polarised, characteristics which are effectively filtered out by the criteria that ensure quasi-linear polarisation.

Other types of structures, such as fast mode waves, have similar polarisation and compressional characteristics as 'true' 165 MMs. They are usually observed at Mars when the exosphere is particularly extended and neutral hydrogen densities significantly increase, that is, around perihelion for Ls = 251° and during the dust storm season for Ls = [135°–225°](Mazelle et al.,

6

2004; Halekas et al., 2020). These waves are linked to pickup ion processes, in the case of the quasi-parallel shock. Consequently, when one looks only at the magnetic field, strong fluctuations ($\Delta|\mathbf{B}|/B_{bg} \geq 0.1$) may appear, which are not sinusoidal and have a quasi-linear polarisation, without these structures necessarily being MMs.

170   In all of the previous cases, magnetic field intensity and plasma density will typically be in phase, as opposed to the expected MM behaviour (Hasegawa, 1969). However, this information is sometimes neither available at the desired high time resolution nor practical to derive as in large statistical surveys. We suggest here two mitigation strategies: (1) making sure that the magnetic field across the structures' region does not rotate more than 10–20°, as theoretically predicted for MMs (Treumann et al., 2004) and in agreement with past observations (Tsurutani et al., 2011), and (2) restricting the detections to magnetosheath conditions

175   only and excluding the region around the bow shock to avoid these foreshock transients.

Strategy (1) constrains the detected structures to behaviours more reminiscent of MMs: we apply Criterion 5 of Table 1 which ensures that the magnetic field does not rotate significantly across the structure. From the magnetic field vector in MSO coordinates, magnetic azimuth and elevation angles are defined as:

$$az = \arctan\left(B_y/B_x\right) \quad \text{and} \quad el = \arctan\left(B_z/\sqrt{B_x^2 + B_y^2}\right) \tag{3}$$

180   First, we define so-called 'regions' containing structures detected within a maximum of 30 s between one another, ignoring isolated singular events; two separate regions are thus more than 30 s apart. In this way, some of these discarded isolated events are not part of the usual quasi-periodic train of MM structures, and thus are more reminiscent of the so-called 'linear magnetic holes' (LMH), in the original definition of Turner et al. (1977), structures that we want to filter out from the database. The particular value of 30 s was chosen empirically as double the length of the longest MM structures found at Mars or Venus (see

185   for example Simon Wedlund et al., 2022c; Volwerk et al., 2008, 2016); moreover this ensures that rotations could be calculated for trains of MM-like structures for which the 2-min windowed background magnetic field values would be representative. We then estimate how much azimuth and elevation angles fluctuate at the detected position of the candidate structure by calculating their running standard deviation $\langle\sigma(az, el)\rangle$ over a 2-min sliding interval, keeping only those structures where $\langle\sigma(az, el)\rangle$ is less than 10° for each angle (Simon Wedlund et al., 2022c).

190   Complementarily, Strategy (2) may make use of the position of the bow shock crossing in the spacecraft data and ignoring the detected structures in a range of radial distances around it (or equivalently, in a range of durations around the time of the crossing). For this part, we use the automatic bow shock detection technique explained in Simon Wedlund et al. (2022b), who used a predictor-corrector algorithm based on magnetic field measurements only at Mars. Their list of automatically detected crossings is freely available (Simon Wedlund et al., 2022a). It discriminates between (*i*) crossings from the solar wind into the

195   magnetosheath and from the magnetosheath into the solar wind, and (*ii*) Q-⊥ and Q-∥ bow shock crossings. The latter aspect is useful for investigating how the shock configuration impacts the spatial distribution of MM-like structures (see Section 2.3). It is important to note here that the technique of Simon Wedlund et al. (2022b) is biased towards the detection of Q-⊥ crossings as it is based on the classic **B**-field signature of the quasi-perpendicular shock, with clearly defined foot, ramp and overshoot. Between 2014 and 2021 of MAVEN operations, Simon Wedlund et al. (2022b) recorded a total of 11,967 Q-⊥ and 2,962 Q-∥

200   'clear' crossings, discarding 1,615 crossings where the shock signatures were difficult to automatically ascertain. In addition,

**Table 2.** Total numbers of MM-like structures $N_{MM}$ detected at Mars, according to the criteria of Table 1, incrementally, from 1 Nov. 2014 to 7 February 2021 with the MAVEN/MAG instrument. RIE means "removal of isolated events". The most drastic decrease in $N_{MM}$ occurs when including the criterion on magnetic field azimuth and elevation angles, which should not change across a given structure by more than $20°$ (Criterion 5).

| Criteria | $N_{MM}$ | Difference | Decrease | Comment |
|---|---|---|---|---|
| 1–4 | 2,046,533 | – | – | Original database |
| 1–4 + 5 | 307,614 | $-1,738,919$ | 85% | Large angular fluctuations removed |
| 1–4 + 5 + RIE | 283,792 | $-23,822$ | 8% | Isolated events removed |
| 1–4 + 5 + RIE + 6 | 176,041 | $-107,751$ | 38% | Shock and solar wind structures removed, Final database |

knowing where the shock is can be used to automatically ensure that the structures are located in the magnetosheath. In turn, this naturally fulfills Criterion 6 in Table 1, where the background magnetic field $B_{\mathrm{bg}}$ needs to be two times higher than the average, but highly variable, interplanetary magnetic field $B_{\mathrm{imf}}$.

In practice, knowing when the bow shock crossing took place, we first identify in spacecraft ephemerides the portion of the

205  orbit in the solar wind as opposed to inside the bow shock structure. Then, we remove all MM-like structures that are closer than $0.075\,R_M$ ($\sim 250$ km) to the shock position, assuming that those are shock substructures, situated immediately upstream, at or downstream of the shock itself. This value was chosen empirically from a subset of orbits with magnetic fluctuations that were incorrectly captured by the original detection algorithm (see for an illustration Fig. 1).

Table 2 displays the number of MM-like structures detected when incrementally applying the criteria of Table 1, together

210  with the two mitigation strategies discussed above. From the original $\sim 2 \times 10^6$ MM-like events detected in Section 2.2.1, Strategy 1 (using Criteria 5 and ignoring $23,822$ isolated events) removed 85% of the total number of events: we end up with only $283,792$ MM-like detections. Criterion 5 is the criterion that removes most of those events due to the harsh constraint on the stability of the magnetic field angular fluctuations within trains of MM-like structures. It shows moreover that Criterion 5 is of utmost importance to remove from the database candidates that are not linearly polarised. Applying Strategy 2 to filter out

215  shock substructures and solar wind magnetic holes (based on Criteria 6 and an automatic estimate of the position of the shock) removes another $107,751$ events, resulting in a total of $176,041$ MM-like events in our final database.

### 2.2.3 Examples and caveats of the method

Figures 1 (high solar activity conditions) and 2 (low solar activity) show examples of MM-like detections, with total magnetic field and Criteria 1–4 of Table 1. Detections matching Criteria 1–4 in coincidence are shown as vertical grey and green lines,

220  with the green lines marking the final detections with the removal of false positives (Criteria 1–4 and 5–6 in coincidence).

The events of 8 Sept. 2016 (Fig. 1) occur at and in the wake of a predominantly quasi-perpendicular bow shock crossing, with angle $\theta_{\mathrm{Bn}}$ between the normal to the shock surface and the average interplanetary magnetic field (IMF) direction of about $80°$. Comparison of magnetic field and density variations is displayed in the bottom panel, with magnetic field (left axis, blue) and density (right axis, red) fluctuations being in antiphase when $\Delta B/|B|$ and $\Delta N/N$ have opposite signs. For the detections in

225  grey in the ramp of the shock as initially captured by Criteria 1–4 but without removal of false positives, $B$ and $N$ appear mostly in phase at the cruder resolution of the SWIA instrument (here 8 s, with $\Delta B/|B|$ and $\Delta N/N$ having most of the time the same sign in the bottom panel). This implies a false positive detection: further applying Criteria 5–6, they are correctly removed from the final database, leaving only the structures in green. The structures in green display a more marked $B - N$ antiphase behaviour (bottom panel), although some of the shorter detected structures may seem to be in phase; this is however difficult

230  to unambiguously ascertain owing to SWIA's 8-s resolution which cannot capture these shorter magnetic field structures. The temperature anisotropies responsible for the generation of MMs are expected to take place in the wake of a quasi-perpendicular shock (see Hoilijoki et al., 2016). Consequently, this event, together with the one discussed in Simon Wedlund et al. (2022c) (24 December 2014 around 11:25 UT, also at high solar activity), are 'textbook' examples of MM occurrences.

In Fig. 2 (23 Mar. 2019), detections occur in the solar wind region around 19:15 UT (not shown) and in the magnetosheath

235  towards the IMB around 18:38 UT, behind a predominantly quasi-parallel shock ($\theta_{\mathrm{Bn}} \approx 25°$). Multiple crossings of the shock from the magnetosheath into the solar wind take place. The automatic estimate of the shock's location following Simon Wedlund et al. (2022b) pinpoints the last great magnetic field enhancement around 19:05 UT, whereas the magnetosheath-to-solar wind position is visually closer to 18:52 UT: this is due to that automatic estimate choosing the last occurrence of a shock-like structure when crossing from the magnetosheath to the solar wind. In the solar wind after 19:05 UT, magnetic field and density

240  seem mostly in phase: two 'linear magnetic hole' (LMHs) candidates (not shown) are first captured by Criteria 1–4. After they are removed from the database using Criteria 5–6, only MM-like structures which are roughly in $B - N$ antiphase (around 18:39 UT) are kept.

That said, other events deeper in the magnetosheath (around 18:33 and 18:36 UT) and part of the database in grey are also removed because they are isolated structures: the second of these events around 18:36 UT presents a clear $B - N$ anticorrela-

245  tion. This shows that although the detection method using Criteria 1–6 appears quite apt at detecting MM-like structures and removing structures that are clearly not MMs, it may also ignore promising candidates. Conversely, we also expect the method to keep structures that are likely not MMs but situated in the magnetosheath (with $B$ and $N$ in phase). For illustration, isolated 1-s events, discarded in the final database, amount to 23,822 additional events, which make about 14% of the final total number of events (see Table 2). As a consequence, on this criterion only (isolated structure), the frequency of MM-like detections in

250  our final database could be underestimated by at least 10%.

Another aspect is that several individual structures as part of trains of MMs are likely to have been missed by our $B$-field-only method: see for example on Fig. 2, around 18:35 UT where clear $B$-$N$ anticorrelations are not captured even by the original detection method. This is an inherent caveat of any automatic detection method based on somewhat arbitrary thresholds and a possibly flawed estimate of the background field (see Joy et al., 2006, who used upper and lower quartiles of $B$ to overcome

255  some of this difficulty). Choosing laxer detection criteria would increase the likelihood of capturing such structures; however this would also be at the expense of increasing false positive detections.

Finally, we only consider in our study so-called 'linear' MM-like structures. As shown in studies made in the Earth's magnetosheath (Génot et al., 2001, 2009), MMs can have many different polarisations, with elliptically polarised structures being found more often than linearly polarised ones. A discrimination between all polarisations states is difficult to achieve

260   with **B**-field-only criteria and is outside of the scope of our study. Therefore, our method may miss a substantial amount of
structures which are MMs but are non-linearly polarised in nature.

Several tests have been made on reduced datasets to find the 'sweet' spot of all criteria gathered in Table 1 (see also the
discussion in Simon Wedlund et al., 2022c) to keep as many confirmed MM-like structures as possible whilst avoiding other
compressional structures that are not MMs. This points overall to the difficulty of characterising such structures reliably with
265   magnetometer-only data. In all cases, after applying our mitigation strategies, the number of structures that are captured is
thus most likely a lower estimate of the frequency of linearly and non-linearly polarised MM-like structures. As shown in
Figs. 1 and 2, one way to mitigate these aspects is to check for the antiphase behaviour between $B$ and $N$ (at 4–8 s resolution),
at the expense of the smaller MM-like structures. This is outside the scope of our current work which aims at evaluating the
$B$-field-only method of detection; using the full plasma instrumentation on board MAVEN is thus left to a future study.

## 2.3   Mapping technique

Calculating MM-like occurrence probabilities and mapping them in the magnetosheath of Mars proceed as follows.

### 2.3.1   Detection probability

First, we apply the $B$-field-only criteria of Table 1 in coincidence to the whole MAVEN dataset, from November 2014 to
February 2021. This yields the timing and duration of MM-like structures, noted $t^{\mathrm{struct}}$ and $\Delta T^{\mathrm{struct}}$, respectively. It is important
275   to remark here that a full dip or peak of any given MM-like structure is usually longer than the total sum of 1-s detections for
that structure. This arises from the fact that all the criteria of Table 1 must be simultaneously met to validate this as a detection.
Consequently, $\Delta T^{\mathrm{struct}}$ can only be an underestimate of the total duration of a structure, which we expect to be about 25%, as
evaluated from visual comparisons in a subset of events (see Figs. 1 and 2).

Second, we define a spatial grid for the data accumulation. We start with spacecraft coordinates expressed in the Mars Solar
280   Orbital (MSO) coordinate system (sometimes called "Sun-state" coordinates), where the $X_{\mathrm{MSO}}$ axis points towards the Sun
from the centre of Mars, $Z_{\mathrm{MSO}}$ points towards Mars' North pole and is perpendicular to the orbital plane defined as the $X_{\mathrm{MSO}}-$
$Y_{\mathrm{MSO}}$ plane passing through the centre of Mars, with $Y_{\mathrm{MSO}}$ completing the right-hand triad. We then transform this system into
aberrated MSO coordinates by rotating the $X_{\mathrm{MSO}}-Y_{\mathrm{MSO}}$ plane 4° counterclockwise around the $Z_{\mathrm{MSO}}$ axis in order account for
the apparent "aberration" of the orbital motion of Mars with respect to the average direction of the solar wind (Simon Wedlund
285   et al., 2022b). The new aberrated coordinate system, aligned with the average apparent solar wind direction, is noted $X'_{\mathrm{MSO}}$,
$Y'_{\mathrm{MSO}}$ and $Z'_{\mathrm{MSO}}$ (although $Z'_{\mathrm{MSO}} = Z_{\mathrm{MSO}}$ by construction). For brevity, the $+X'_{\mathrm{MSO}}$ ($-X'_{\mathrm{MSO}}$) direction is sometimes referred to
as "subsolar" ("antisolar") direction in the following, although strictly speaking, they should be referred to as "subsolar-wind"
and "antisolar-wind" directions.

A two-dimensional cylindrical coordinate grid can then be created, with the abscissa $i$ along the $X'_{\mathrm{MSO}}$ axis and the ordinate $j$
290   defined as $\sqrt{Y'^{2}_{\mathrm{MSO}} + Z'^{2}_{\mathrm{MSO}}}$. The grid resolution is chosen so that, on average, the residence time of the spacecraft in each grid cell
is large enough in all cells covered by the spacecraft's orbit. For example, for Mars (average planetary radius $R_M = 3389.5$ km)
and applied to MAVEN ephemerides, a resolution of $\Delta R = 0.05 R_M$ ensures that the spacecraft residence time in each $(i, j)$

cell is of the order of $500 - 1000\,\mathrm{s}$ ($8 - 16\,\mathrm{min}$) per grid cell for a typical Mars year of 687 Earth days; for a resolution of $\Delta R = 0.1\,R_M$, average residence times are of the order of $5 \times 10^4$ s ($\sim 14$ hours). The latter resolution of $\Delta R = 0.1\,R_M$ is thus
295   chosen to maximise the statistical significance of the MM-like detections. Examples of spacecraft residence times with this grid resolution are shown in Fig. 8, left panels, for several consecutive Mars years.

We can now define the probability $\mathcal{P}$ of detecting MM-like structures in a chosen spatial grid cell $(i, j)$ as the total duration of the detected structures $\Delta T^{\mathrm{struct}}$ divided by the accumulated residence time of the spacecraft $\Delta T^{\mathrm{sc}}$ (see also Volwerk et al., 2016):

$$\mathcal{P}(i, j) = \frac{\sum_k \Delta T_k^{\mathrm{struct}}(i, j)}{\Delta T^{\mathrm{sc}}(i, j)}, \tag{4}$$

with $k$ the number of structures found in each grid cell $(i, j)$. In other words, $\mathcal{P}$ represents the percentage of observations containing a MM-like structure at any given point in the magnetosheath. The accumulation of the structures in the grid, including those crossing a cell boundary, is naturally taken into account using a bi-variate histogram accumulation.

An example of spacecraft residence time and MM-like detection probabilities is shown in Fig. 3a,b. Figure 3 is discussed
305   further in Section 3.1. As mentioned above, because $\Delta T^{\mathrm{struct}}$ is a likely underestimate of the total duration of MM-like structures in the magnetometer dataset, $\mathcal{P}$ is also underestimated: we thus refer to it as a 'detection probability' of detecting MM-like structures.

### 2.3.2 Characterisation with respect to physical parameters

To study how the distribution of MM-like structures varies during the time of the mission, we choose several controlling
310   physical parameters, which are summarised in Fig. 4. We discriminate our results against:

1. Mars Year (MY): on average, one MY lasts 1.88 Earth years (687 Earth days). Because MAVEN started its scientific investigation in November 2014, we consider data from this date (after the autumn equinox of MY32) up to MY35 (ending on 7 Feb. 2021). Precise start and end times for each MY were obtained from the equation of time of Allison and McEwen (2000) (their Equation 14). For reference, MY32 = [31 Jan. 2013–18 Jun. 2015[, MY33=[18 Jun. 2015–05
315      May 2017[, MY34=[05 May 2017–23 Mar. 2019[, MY35=[23 Mar. 2019–07 Feb. 2021[.

2. EUV flux levels: following Halekas et al. (2017b) and Gruesbeck et al. (2018), we use two EUV flux levels, one "high" for EUV fluxes $I_{\mathrm{EUV}} \geq 0.00277\,\mathrm{W\,m^{-2}}$, one "low" for fluxes $I_{\mathrm{EUV}} < 0.00277\,\mathrm{W\,m^{-2}}$. This limit is the median of the EUV flux in the 2014–2021 period as calculated from FISM-IUVS' daily irradiance at 121.5 nm (Lyman-$\alpha$ line), itself derived from the Mars EUVM model (Thiemann et al., 2017). It is also close to the threshold value of $= 0.0029\,\mathrm{W\,m^{-2}}$
320      considered by Gruesbeck et al. (2018) for the first year of MAVEN observations. During the time of the mission, the solar activity went from medium to low (from MY32 to MY34) followed by a slight recovery during MY35; local peaks in the measured EUV flux correspond to perihelion conditions and local dips to aphelion conditions (see Fig. 4).

3. Solar longitude (Ls): Ls measures the position of a planet in its orbit around the Sun. Because Mars has a relatively high orbital eccentricity ($\epsilon = 0.0935$) and is tilted $25.2°$ with respect to its orbital plane, Ls is also a measure of atmospheric

325       seasons. Ls = 251° (Ls = 71°, respectively) corresponds to perihelion (aphelion) conditions. In this study, we use four
          ranges centred on equinoxes and solstices: Ls1 = [315°–45°] (Northern Hemisphere [NH] spring equinox), Ls2 = [45°–
          135°] (NH summer solstice), Ls3 = [135°–225°] (NH autumn equinox), Ls4 = [225°–315°] (NH winter solstice). Season
          timings were also obtained from Allison and McEwen (2000) (their Equations 15–19). See Fig. 4 for the centred seasons
          with respect to time.

330  As discussed in Halekas et al. (2017b) and Simon Wedlund et al. (2022b), each controlling parameter is co-dependent on other
     parameters. The Martian atmosphere depends on a complex interplay between heliocentric distance, axial tilt, and atmospheric
     circulation (Dong et al., 2015). At perihelion (Ls = 251°), the solar EUV flux is largest (see Fig. 4) and causes the Martian
     exosphere to progressively heat up and significantly expand (Forbes et al., 2008). In their study of the hydrogen (H) exosphere's
     seasonal variability, Halekas (2017), confirmed by Halekas and McFadden (2021), found a peak of H column density around
335  the NH winter solstice (Ls = 270°), suggesting either a degree of latency in the exosphere's response to solar inputs, a seasonal
     component due to lower atmosphere dynamics, or both. Simultaneously to these complex changes, increased EUV fluxes lead
     to increased ionisation in the ionosphere and in the exosphere far in the upstream solar wind (increased charge exchange and
     pickup ion process), leading to the induced magnetospheric obstacle to the solar wind to grow in size (Hall et al., 2016, 2019).
     Consequently, one Ls bin (representing a Martian season) encompasses effects arising from several mechanisms affecting the
340  extent of the exosphere and that of the Mars plasma environment (Yamauchi et al., 2015): global atmospheric circulation,
     presence of dust storms or EUV inputs, themselves a function of heliocentric distance and solar cycle (Trainer et al., 2019).
     Similarly, any given Mars year includes variations in atmospheric seasons and EUV flux (since the solar EUV flux varies
     significantly with heliocentric distance, to which the solar activity variations are superimposed). Either Mars years, Ls or EUV
     flux levels indiscriminately contain all bow shock geometries, Q-∥ or Q-⊥ alike.

345  For each of the above controlling parameters, external drivers include the highly variable solar wind inputs, such as dynamic
     pressure and Mach number (Halekas et al., 2017b). This makes it all the more difficult in practice to isolate the role of a single
     controlling parameter from the others. For example, one way to help disentangle these effects would be to study the seasonal
     changes at a fixed EUV flux level or, inversely, to study a EUV flux level at a fixed seasonal bin. However, depending on the
     chosen binning, the event statistics may become too low for a statistically significant interpretation. We leave this for a future
350  study, when MAVEN will have completed several additional MYs, and choose a complementary approach using the probability
     density function (PDF) of the total number of detected structures as a guide (see Section 3.2.1).

     Table 3 presents the general statistics of our MM-like structure database, with a total of 176,041 events detected between
     1 Nov. 2014 and 7 Feb. 2021 (last day of MY35), with a total residence time of the spacecraft in the grid of about 6.1 Earth
     years. For each controlling parameter we also calculate the residence time and global observation ratio of MM-like structures.
355  In Sect. 3, we will discuss the significance of these ratios and contrast them against the detection probability maps.

**Table 3.** Statistics of MM-like structure found from 1 Nov. 2014 to 7 February 2021 with the MAVEN/MAG instrument, following the detections performed in Section 2.2 and for different cases. $N_{\mathrm{MM}}$ represents the total number of MM-like events found (equivalent to a duration in s because of the magnetometer resolution of 1 s), whereas $\Delta T_{\mathrm{tot}}^{\mathrm{sc}}$ is the total duration that the spacecraft spent orbiting Mars during that time. Ratios $N_{\mathrm{MM}}/\Delta T_{\mathrm{tot}}^{\mathrm{sc}}$ are given in percentages.

| Case | $N_{\mathrm{MM}}$ | $\Delta T_{\mathrm{tot}}^{\mathrm{sc}}$ [s] | Ratio [%] |
|---|---|---|---|
| MY32 | 14,285 | 18,005,770 | 0.079 |
| MY33 | 58,584 | 59,120,895 | 0.099 |
| MY34 | 50,315 | 59,188,581 | 0.085 |
| MY35 | 52,857 | 56,662,768 | 0.093 |
| EUV flux $\geq 2.77\,\mathrm{mW\,m^{-2}}$ | 88,688 | 105,764,081 | 0.084 |
| EUV flux $< 2.77\,\mathrm{mW\,m^{-2}}$ | 87,353 | 87,213,933 | 0.100 |
| Ls1 = [315° − 45°] | 49,497 | 52,184,340 | 0.095 |
| Ls2 = [45° − 135°] | 56,591 | 51,082,098 | 0.111 |
| Ls3 = [135° − 225°] | 36,928 | 41,449,456 | 0.089 |
| Ls4 = [225° − 315°] | 33,025 | 48,262,120 | 0.068 |
| All | 176,041 | 192,978,014 | 0.091 |

## 3 Results: mapping MM-like occurrence around Mars

We now present the statistics and the 2D cylindrical coordinate occurrence maps of MM-like structures in the magnetosheath of Mars resulting from our automatic detections described in Sections 2.2 and 2.3.

### 3.1 Overview of the full dataset

360  Figure 5 shows the probability density function (PDF) of several characteristic quantities for the 176,041 MM-like structures detected from 1 Nov. 2014 to 7 Feb. 2021 (MY32 to MY35): magnetic field intensity $|\mathbf{B}|$ (panel a) as well as those of Criteria 1–4 inside the structures (panels b to f). For each, we indicate the bin position of the peak of the distribution. Most detected structures exhibit characteristics that are close to the criteria threshold values (panels b, c and e). The eigenvalue ratios extracted from the MVA (panels e and f) show that the variance ellipsoid is cigar-shaped, although not exceedingly so, with most values

365  having $\lambda_{\mathrm{max}} \geq 2.5\lambda_{\mathrm{int}}$ and $\lambda_{\mathrm{int}} \geq 1.6\lambda_{\mathrm{min}}$. The variance ellipsoid is also oriented along the average background magnetic field direction, as shown in panels (c) and (d), with most values having $\Theta_{\mathrm{maxV}} \lesssim 18°$ and $\Phi_{\mathrm{minV}} \lesssim 89°$. Together, these criteria make sure that the structures are highly compressional and quasi-linearly polarised, as expected from MMs.

The spatial distribution of the detected structures is shown in Fig. 3 as maps for the full dataset considered here, with a bin resolution of 0.1 $R_M$. For reference, we also indicate the bow shock (BS) and the induced magnetospheric boundary (IMB,

370  sometimes referred to as 'magnetic pileup boundary') from several previous works (Edberg et al., 2008; Hall et al., 2019; Simon Wedlund et al., 2022b). Because these boundary positions were determined statistically and represent an average over an extensive range of geophysical conditions, their exact position may vary by a few grid cells for individual observations and

should only be taken as a rough indicator of the shape of the boundaries around that point. Figure 3a displays the residence

time of the spacecraft $\Delta T^{\mathrm{sc}}$: on average, MAVEN spends about $1.6 \times 10^5$ s (18.5 days) in each cell with a very homogeneous

375 coverage throughout, except in the subsolar region in the upstream solar wind and in the deep magnetospheric tail in the

antisolar-wind direction. The regions of maximum orbital coverage are close to the IMB and around the terminator plane in

the magnetosheath.

The spacecraft residence time $\Delta T^{\mathrm{sc}}$ is then used as a normalising factor to calculate the probability $\mathcal{P}$ of detecting MM-like

structures (Fig. 3b), expressed here in percentage and in logarithmic scale. Because of relatively poorer spacecraft coverage

380 in the antisolar and subsolar directions, $\mathcal{P}$ may reach artificially high values in those regions: this is especially visible at

coordinate $(1.1–1.5, 0) R_M$ on panel (b). MM-like structures are mostly confined to two main regions, one in the immediate

vicinity of the predicted shock (at SZA > 45°), and one in the magnetosheath pressed against the IMB. Both of these regions

have $\mathcal{P} > 0.2\%$ with maximum values of 0.5–0.8% reached in the subsolar region of the magnetosheath, close to the IMB. A

third region can be identified in the magnetospheric tail, where occasional high probabilities are encountered. Qualitatively,

385 this is very similar to the results of Ruhunusiri et al. (2015), who showed that MM waves were predominantly present in

MAVEN's first year of operations in the deep magnetosheath and in the tail. They reported average occurrence ratios of less

than 10% somewhat uniformly distributed in the volume of space, with peaks between 10 and 25% occurring in three main

regions: the middle of the magnetosheath for SZA ≈ 80°, closer to the IMB for SZA ≈ 60° and in the magnetospheric tail inside

the statistical IMB. Although our main detection regions are similar to those of Ruhunusiri et al. (2015), both in position and

390 shape, we report here much lower absolute detection probabilities of MM-like structures (maximum of 0.8%). A quantitative

comparison with the values of Ruhunusiri et al. (2015) is however difficult because of several factors. Firstly, our detections

cover a much longer time span than those of Ruhunusiri et al. (2015), undergoing quite different solar conditions. Secondly,

the two detection methods differ significantly: our $B$-field-only criteria detection permits us to capture trains of short events

with 1-s resolution at the expense of an ambiguity in the nature of the detected structure, whereas Ruhunusiri et al. (2015) used

395 wave analysis techniques based on transport ratios with a cruder time resolution (4–8 s with a Fourier transform on consecutive

128 s intervals). Moreover, the strategies we applied to help remove possible false positive detections may have filtered out

legitimate events to a certain extent. Finally, as explained in Section 2.3.1, the total duration of MM-like structures $\Delta T^{\mathrm{struct}}$ is

underestimated in our approach by about 25% because of inherent limitations in the detection method. All points combined,

this implies that the detection probability should be seen as a lower estimate (see Section 2.2.2).

400 In contrast to the two main high-probability regions discussed above, we identify a region of low probabilities in the portion

of the sheath behind the terminator plane and in the tail, where $\mathcal{P} < 0.1\%$. We hypothesise that this is due to the plasma

flow configuration which may preferentially transport the MMs almost unchanged from their birth region behind the quasi-

perpendicular shock down to the IMB and along it.

Quantitatively, these results are in line with studies at Venus (Volwerk et al., 2016; Fränz et al., 2017), which registered

405 detection probabilities of less than 5% on average, with maxima of occurrences taking place immediately behind the shock

and close to the IMB. As in our results, these authors also pointed out increased occurrences in the magnetospheric tail.

It is important to remark here that the average modelled position of the shock appears on Fig. 3b to fall in the middle of

the distribution; however, because we removed shock substructures from the dataset (see Section 2.2.2) and considered only magnetosheath events, all of the events shown here are in effect in the magnetosheath and not in the solar wind. This attests to the high variability of the shock position and the limitations of a single modelled curve to represent accurately the position of the shock, a conclusion in conformity with dedicated studies (Gruesbeck et al., 2018).

Magnetic field compressional fluctuations $\Delta|\mathbf{B}|/B_{\mathrm{bg}}$ for the detected events are next shown in Fig. 3c. Following Criterion (1), we consider only structures with $\Delta|\mathbf{B}|/B_{\mathrm{bg}} \geq 0.15$. Fluctuations are comparatively higher in the magnetosheath ($\Delta|\mathbf{B}|/B_{\mathrm{bg}} > 0.25$) and relatively low in the magnetosphere (delimited by the average IMB, with $\Delta|\mathbf{B}|/B_{\mathrm{bg}} \leq 0.20$). More precisely, some of the largest magnetic fluctuations occur close to the terminator plane around the shock and in the subsolar magnetosheath closing in on the IMB, with values often reaching 0.4 and above. Median fluctuations are $0.25 \pm 0.03$ for the detected structures at the chosen grid resolution. In the magnetosphere's tail, certain cell-by-cell fluctuations are quite abrupt from low to high values, in part due to the increasingly poor orbital coverage in this region.

Figure 6 displays the daily detection rate of MM-like structures during the entire mission. On average throughout MY32 to MY35 with MAVEN, we find $\langle N \rangle = 68 \pm 43$ structures per day (ignoring single isolated 1-s events, see Sect. 2.2.2) fulfilling the criteria of Table 1. Because of the MAG resolution chosen, this represents 68 s of detected structures per day, or 2.8 detections per hour. Large departures from the 7-day average in red can be seen, but they appear to steadily decline over time. This behaviour coincides with a progressive decline of EUV flux and solar activity at Mars during that period (compare with Fig. 4). As a comparison, the mean daily detection rate over each MY changes little (green dotted line on the figure), with MY33 having more detections (85 structures/day in mostly high EUV flux) than any other year, and MY34 (73 structures/day in mostly low EUV flux) having least detections. MY32 seems to be an outlier, but considering that we probed only the later portion of the full MY, we cannot compare absolute detection numbers with the other MYs without first normalising to the spacecraft's residence time during that period.

Finally, if we assume that most structures last $5 - 10$ s on average, we end up with $68/10$–$68/5 \approx 7$–14 MMs/day in Mars' magnetosheath. Incidentally, this is larger (but still within the same order of magnitude) than frequencies of large linear magnetic holes (LMHs) recorded upstream of the Martian bow shock (2.1 LMHs/day, Madanian et al., 2020, as measured with MAVEN over a period of 3 months).

## 3.2 Spatial dependence on physical parameters

Spatial maps of MM-like structures around Mars detected with MAVEN using magnetic-field measurements are discussed below with respect to the controlling parameters expounded in Section 2.3.2. Before examining these in more detail, we present a few considerations based on their probability density function (PDF).

### 3.2.1 Probability density functions (PDF)

Figure 7 presents the PDF of the detected MM-like structures with respect to radial polar coordinate $\rho = \sqrt{X'^2 + Y'^2 + Z'^2}$ (panels a and d, in bins of $0.1 R_M$ which is the resolution of our 2D distribution maps), EUV flux levels (panels b and e, in bins of $0.1\,\mathrm{mW\,m^{-2}}$, and Ls (panels c and f, in bins of $10°$). Each PDF is discriminated against high and low solar flux levels (panels

a-c) and against Ls ranges (panels d-f, with Ls1–4 for NH spring, summer, autumn and winter) to illustrate the co-dependence of the studied parameters. Panels (b) and (f) represent the baseline statistics of $I_{EUV}$ and Ls parameters. They highlight the bins where the PDFs have larger values and hence the parameter has a good statistical coverage. For example, the sharp drop in PDF occurring for $I_{EUV} > 3.4\,\mathrm{mW\,m^{-2}}$ in Fig. 7b is due to the smaller spacecraft orbital coverage above this threshold: this

445  is also clearly seen in Fig. 4, where only MY32 and MY33 contribute to the statistics, with the threshold $\langle I \rangle$ just above the irradiance local peaks during MY34 and MY35. Successive Ls ranges are in contrast quite homogeneously distributed with relatively constant PDFs throughout (Fig. 7f), with the Ls2 range having the largest PDF overall.

In Fig. 7a/d, we see a combined peak of the PDFs in the $1.2 - 1.3\,R_M$ bins, close to the position of the IMB ($R_{ss,imb}$ = 1.25–1.33 and $R_{td,imb} \sim 1.45$, see Trotignon et al., 2006; Edberg et al., 2009). The PDF drops by almost half around $1.5\,R_M$, roughly

450  $0.2\,R_M$ ahead of the bow shock's variable subsolar position. Hence, a rather homogeneous ring of MM-like structures around the planet forms, centred on $1.2 - 1.3\,R_M$, as already seen in Fig. 3. Overall, the distributions look very similar for all EUV and Ls ranges considered. However, we see two more prominent peaks of the PDF, one $0.1$–$0.2\,R_M$ inwards of the terminator standoff distance $R_{td}$ (true for all EUV conditions and Ls ranges), the other $0.2\,R_M$ outwards of it (low EUV conditions, Ls2 contributing most, Ls4 the least due to reduced spatial coverage of MAVEN in these conditions). These two peaks correspond

455  in Fig. 3 to the tail detections around $2.3\,R_M$ from the centre of Mars, and to the detection enhancement around the average shock position in the terminator plane around $3\,R_M$.

The co-dependence between EUV flux and Ls range is clearly seen in Fig. 7c/e. Obviously, aphelion and perihelion conditions mostly correspond to PDFs for low and high EUV solar fluxes, respectively. The main peak in the PDF appears in bin Ls = $80 - 90°$ within the 'Ls2' range (see also Fig. 7f), slightly after aphelion conditions. No peak in the PDF particularly

460  stands out for Ls > 180° and higher EUV fluxes, although a relatively lower PDF seems to occur around perihelion conditions. Complementarily, in Figs. 7f and 7e, range Ls2 (Ls = 45–135°, containing aphelion conditions) is dominated by low EUV fluxes, whereas Ls4 (Ls = 225–315°, containing perihelion conditions) is dominated by high EUV flux, the first range strongly peaking at $I_{EUV} \sim 2.3\,\mathrm{mW\,m^{-2}}$, the second range at $I_{EUV} \sim 3.3\,\mathrm{mW\,m^{-2}}$. Consequently, these two Ls ranges appear to be a good proxy of conditions driven by seasons only at an almost constant EUV flux, either low, or high. The remaining two Ls

465  ranges, Ls1 (Ls = $315 - 45°$) and Ls3 (Ls = $135 - 225°$), have similar distributions with respect to EUV flux, and are thus more comparable to one another.

Overall, these preliminary results are consistent with past observations at Mars, be it with MGS (Bertucci et al., 2004) or with MAVEN (Simon Wedlund et al., 2022c), who all noted that MM structures seemed to pile up against the IMB. This suggests that MMs, after being created upstream of their detection place, are convected down to it with the ambient plasma

470  flow. Using the full MAVEN plasma complement and owing to the ambient plasma becoming less unstable to MMs the further away from the shock, the locus of generation of the MMs found by Simon Wedlund et al. (2022c) was inferred to be in the immediate wake of the quasi-perpendicular shock, a condition that seems to predominate in the 2014–2021 MAVEN dataset (Simon Wedlund et al., 2022b).

### 3.2.2 Dependence on Mars Year

475 Figure 8 presents, for four MYs (panels a–d), the spacecraft residence time (left panels), the MM-like detection probability $\mathcal{P}$ (middle panels), and their relative difference (right panels) with respect to the total detection probability $\mathcal{P}_{tot}$ (taken from Fig. 3b), in the same format as in Fig. 3. Because MAVEN started observing late in Oct. 2014 (towards the end of MY32), the statistical coverage for MY32 is lower than for MY33–MY35, with a residence time in a grid cell on average about 3 times less than any other year. Similarly, because of the orbit being more compact around the planet during MY35 (panel d), the mean
480 residence time in a given grid cell is significantly higher than for the other years. However, relatively high residence times above $2 \times 10^4$ s (5.5 hours) ensure a good statistical coverage of the $X' - \sqrt{Y'^2 + Z'^2}$ spatial plane.

The detection probabilities are shown in percentages on the middle panels. For each MY, $\mathcal{P}$ reaches about 1 % at most. The higher probabilities appear close to the IMB in the magnetosheath at SZA angles ranging from the subsolar point (SZA $\approx 0°$) to almost the terminator plane (SZA $\approx 90°$), and in a lesser measure, around the bow shock's predicted position (in effect, in
485 the wake of the true bow shock position). This is in line with our conclusions in Section 3.1. On the rightmost figure panels, negative (positive) percentages are represented by cold (hot) hues for which $\mathcal{P}_{MY} < \mathcal{P}_{tot}$ ($\mathcal{P}_{MY} > \mathcal{P}_{tot}$).

As remarked before, interannual variability of $\mathcal{P}$ at Mars co-depends on EUV flux levels and, to a lesser degree, to exosphere variations (parametrised with Ls), although these latter effects are significantly damped over a full MY. For example, during MY32, the EUV flux levels were always high with MAVEN observing only at high Ls values Ls = [225°–315°]) as shown in
490 Fig. 4. The predominance of red hues especially around the shock (rightmost plot of panel a) points to detections expanding outward under larger EUV fluxes, an effect following the well-known phenomenon of the shock's expansion into the solar wind in those conditions (Gruesbeck et al., 2018; Hall et al., 2019). However, due to the lower statistical orbital coverage during that year compared to MY33–MY35, it is difficult to draw further conclusions on the overall trend of this year's rate.

From MY33 to MY35, less and less detections are seen in and around the shock (less and less red cells on rightmost panels),
495 with MM-like structures mostly confined to a narrow region lodged against the IMB (MY35, middle panels, even factoring the somewhat reduced spatial coverage due to MAVEN's altered orbit in 2019) and in the tail behind the terminator plane (MY33). The slight increase of EUV flux during the second part of MY35 does not seem to be enough to alter this general trend: in effect, global EUV levels for MY34 and MY35 are comparable. Looking more globally into the evolution of the number of detected MM-like events, the ratio of the number of detections to the total time of residence of the spacecraft diminishes from
500 MY33 to MY34 (from 0.099% to 0.085%), followed by a slight increase for MY35 (0.093%, see Table 3). This behaviour mimics well the evolution of the average EUV flux during that time (Fig. 4) and points to a modulating influence of the solar flux in the number of detections, and possibly their spatial distribution, throughout MY33–MY35. From Table 3, the fractional change between MY33 and MY34, and MY34 and MY35 was 0.085%/0.099% = 0.84 (relative decrease in detection rates) and 0.093%/0.085% = 1.09 (relative increase). During that time, the average EUV flux for MY33–MY35 was 2.99, 2.71 and
505 2.74 mW m$^{-2}$, leading to the rather similar fractional changes of 0.90 (MY33–MY34) and 1.01 (MY34–MY35). The influence of the EUV flux on MM detections is further investigated in Section 3.2.3.

As for the mission-wide results, the region containing most MM-like structures spans 2–3 grid cells on average, that is, 0.2–0.3 $R_M$ or $\sim 700 - 1,000\,$km. At the subsolar point, this region fills a significant portion of the narrower magnetosheath. With the predicted position of the IMB from Edberg et al. (2008) for the comparatively higher solar conditions encountered by MGS, MM-like structures seem to "leak" into the magnetosphere, although we cannot say for sure if these detections are in fact inward of the IMB or not. For example, an appreciable part of the detections seemingly present in the solar wind upstream of the average shock position (Hall et al., 2019; Simon Wedlund et al., 2022b) are in fact just behind the actual shock, whose position continuously varies with the solar wind upstream conditions. A cursory examination of individual detections for a reduced dataset in Dec. 2014 and Sept. 2016 pleads in favour of this latter idea (see for example Fig. 1).

### 3.2.3 Dependence on EUV flux

At Mars, variations in EUV flux combine two main aspects: the solar cycle variations on the one hand, and the variations of the EUV input due to the large eccentricity of Mars' orbit on the other (Fig. 4). By modifying the global energy input to the Martian atmosphere-ionosphere-exosphere system, both aspects lead to variations in Mars' exospheric extent and ionisation levels, and are among the key drivers of the bow shock and IMB positions (Hall et al., 2016; Gruesbeck et al., 2018; Simon Wedlund et al., 2022b; Garnier et al., 2022).

More precisely, two combined effects are expected to take place with respect to the generation of MM structures. First, an increased EUV flux favours the expansion of the exosphere in the upstream solar wind, resulting in a swelling of all the plasma boundaries including that of the bow shock (Halekas et al., 2017b). Second, for a given static exosphere, an increased EUV flux also increases the local ionisation in the exosphere, thereby increasing the number of newly born ions and thus pickup ions created (Yamauchi et al., 2015). In turn, these newly picked-up ions may contribute to heating in the perpendicular direction to the magnetic field, helping the plasma to become marginally unstable to the MM instability (MMI < 0, see Price, 1989). These two effects should lead to MMs becoming more frequent and extended in space for higher EUV flux levels, regardless of the nature of the shock.

To study how far this reasoning may hold, we now investigate in Fig. 9 how the EUV flux modifies the detection probability of MM-like structures. We consider two ranges, one for low EUV fluxes ($I_{EUV} < 2.77$ mW m$^{-2}$, panel a), one for high EUV fluxes ($I_{EUV} \geq 2.77$ mW m$^{-2}$, panel b), as previously defined in Fig. 4. To facilitate comparisons between the two conditions, we calculate in panel c the departure from the total detection probability, $\Delta\mathcal{P}_{\text{hi-lo}}/\mathcal{P}_{\text{tot}} = \left(\mathcal{P}_{\text{hi}} - \mathcal{P}_{\text{lo}}\right)/\mathcal{P}_{\text{tot}}$, with $\mathcal{P}_{\text{tot}}$ being the total detection probability from Fig. 3b. A negative percentage (cold hues) implies in this way that $\mathcal{P}_{\text{hi}} < \mathcal{P}_{\text{lo}}$, whereas a positive value (hot hues) implies $\mathcal{P}_{\text{hi}} > \mathcal{P}_{\text{lo}}$.

On average, the spacecraft resides $8 \times 10^4\,$s (22 hours) in a grid cell (left panels), with a very similar spatial coverage except in the solar wind upstream of the bow shock at the subsolar point, and in the deep magnetospheric tail in the antisolar direction. Thus we expect more fluctuations in $\mathcal{P}$ in these regions (middle panels), which can readily be seen in panels (a) and (b). As the exosphere expands with increasing EUV flux, the obstacle to the solar wind flow grows in size, with the bow shock and IMB both swelling up. This is illustrated in Fig. 9 by the dashed bow shock curves of Simon Wedlund et al. (2022b) and how they compare to the fixed curves of Hall et al. (2019).

In Fig. 9c, we observe an outward displacement of the location of high detection probability $\mathcal{P}$ around the bow shock (red region for $X' > 0$), corresponding to the outward displacement of the relevant boundaries with increasing EUV flux. This is consistent with the exosphere comparatively shrinking for low solar EUV flux, with pickup ion effects becoming less prominent around the shock (Mazelle et al., 2004), leading to less MM-unstable conditions there. Because Ls variations are averaged out

545 during a full MY containing all four seasons, the EUV flux thus appears to be the main driver of this tendency. Moreover, the higher the solar activity and the EUV flux, the less events seem present in the deeper magnetosheath and upstream of the dayside IMB (slight dominance of colder hues there in panel c).

This is studied in more detail in Fig. 10 which presents the PDF of the relative difference between high and low EUV conditions ($\Delta\mathcal{P}_{\text{hi-lo}}/\mathcal{P}_{\text{tot}}$ in Fig. 9c), first in the magnetosheath (upstream of the average fitted IMB line of Edberg et al., 2008,

550 panel a), and second in what we term the 'deep magnetosheath' (upstream of the average fitted IMB line and downstream of the shock line of Edberg et al., 2008, panel b), that is, the region between the two continuous black lines in Fig. 9c. The 'deep magnetosheath' distribution is significantly skewed towards low EUV conditions (Gaussian fit peaking at $\Delta\mathcal{P}_{\text{hi-lo}}/\mathcal{P}_{\text{tot}} = -10\%$), confirming our impression from Fig. 9c. In contrast, the 'full magnetosheath' distribution is much more symmetric with a positive skewness but a Gaussian fit peaking at $\Delta\mathcal{P}_{\text{hi-lo}}/\mathcal{P}_{\text{tot}} = -2\%$. The positive skewness is due in part to the large values

555 close to $\Delta\mathcal{P}_{\text{hi-lo}}/\mathcal{P}_{\text{tot}} = 100\%$ corresponding to a geometric effect, that is, the outward displacement of the shock at large EUV conditions; when ignoring these large values, the corrected skewness becomes $-0.01$.

On top of the solar activity-led expansion of the associated plasma boundaries, we thus note from Figs. 9 and 10 that, on average: (*i*) the detection probability in the magnetosheath is perceptibly higher for low EUV flux than for high EUV flux, especially in the near-subsolar magnetosheath and up to about SZA = 45°; and (*ii*) in contrast, detection probabilities appear

560 higher in the tail for high EUV flux than for low EUV flux.

Following Conclusion (*i*), we observe a perceptible decrease of the total detection probabilities with increasing EUV flux, when comparing them to the residence time $N_{MM}/\Delta T_{\text{tot}}^{\text{sc}}$, from 0.100% to 0.084% (see Table 3, from low to high EUV flux). This is in part due to MY32, containing only high EUV fluxes and encompassing perihelion conditions, and for which we calculated noticeably smaller ratios than for other years. However, this conclusion is in direct disagreement with our first expectation that

565 more pickup ions due to higher EUV fluxes would lead to the generation of more MM structures around Mars.

In that aspect, it is useful to compare these maps to similar ones found at Venus for MM-like detections and temperature anisotropy. At Venus, Volwerk et al. (2016) found higher detection levels in the magnetosheath for lower solar activity than at maximum activity. They also noted that the maximum of detection probability moved from just behind the shock at solar minimum down to the IMB at solar maximum. A similar evolution in the spatial distribution of the temperature anisotropy was

570 recently presented by Rojas Mata et al. (2022), with the maxima of anisotropy moving from SZA ≈ 45° to SZA > 60° between solar minimum and solar maximum conditions. In agreement with our findings here with Conclusion (*ii*) at Mars, Rojas Mata et al. (2022) calculated comparatively higher anisotropies in the Venusian magnetospheric tail at solar maximum than at solar minimum. Finally, Rojas Mata et al. (2022) found also that the MM instability criterion was fulfilled significantly more often during solar minimum than during solar maximum conditions, in keeping with the higher detection levels at solar minimum.

575    Our companion paper (Paper II) on the distribution of MM-like structures at Venus further discusses these aspects with the full
Venus Express dataset (Volwerk et al., 2022).

Consequently, Mars and Venus qualitatively display a similar tendency towards higher MM detection probabilities in low
solar activity conditions, a conclusion which appears in contradiction with the addition of pickup ions to the ambient plasma
at higher EUV fluxes.

580    We suggest here two phenomena that likely play complementary roles in enforcing this apparently contradictory trend. First,
Romanelli et al. (2016) have observed an enhanced turbulence due to the presence of so-called proton cyclotron waves (PCWs)
becoming much more prominent the closer to perihelion conditions. This is in turn linked to the local plasma-$\beta$, which plays
a leading role in favouring the MM instability over the Alfvén Ion Cyclotron instability (typically for $\beta \geq 1.5$) as predicted by
the theory of microinstabilities (Gary, 1993). In solar maximum conditions, the plasma-$\beta_\perp$ is on average lower than 1 in the

585    solar wind and in the dayside magnetosheath, as shown by Rojas Mata et al. (2022) for Venus and Wilson III et al. (2018)
for the solar wind. Consequently, the ion cyclotron instability may preferentially grow over MMs, resulting in significantly
less MM detections in solar maximum conditions or for increased EUV fluxes. This would explain why large EUV fluxes
(closer to perihelion conditions) have comparatively lower detection rates of MM-like structures, especially since PCWs have
very different magnetic signatures (non compressional, left-hand elliptically polarised and MVA direction at small angles to

590    background **B**-field direction) and would not be captured by our detection criteria (Delva et al., 2011; Romanelli et al., 2016).
Second, the distributions of pickup ions at Mars and comets are expected to be nongyrotropic (see e.g., Coates et al., 1996;
Coates, 2011; Halekas et al., 2017a), which is known to modify the wave mode properties, the linear growth rate, the instability
threshold and or even produce new wave modes that may consume the additional free energy (see Brinca and Romeiras, 1998;
Motschmann et al., 1997, and references therein). This may in turn favour other modes over MMs, although this specific

595    question remains open. Further study of these two aspects is needed with the use of full plasma suite on board MAVEN; it is
left for the future.

### 3.2.4   Dependence on season (Ls)

Dependence of MM-like structures on Martian season is presented in Fig. 11, with residence times on the left, detection
probabilities in the middle and percentage departures from the total detection probability on the right, as before. In contrast to

600    MY discrimination, the average residence times in a grid cell is quite similar for all four Ls ranges considered, with $\langle \Delta T^{sc} \rangle \sim$
$4.5 \times 10^4$ s (12.5 hours per grid cell), with the smallest residence time for Ls3 = $[135° - 225°]$ (see also Fig. 7g and Table 3).
This is due to a combination of relatively large spatial extension for the orbit and missing that Ls range during MY32 (see
Fig. 4). Conversely, the highest residence time is for Ls2 = $[45° - 135°]$ because of an orbital coverage less spatially extended
in space, and despite the Ls range being also missed during MY32.

605    The detection probabilities $\mathcal{P}$ (middle panels) display a rather similar behaviour for all Ls ranges with two main distribution
loci, one around the shock and the other immediately upstream of the IMB. The Ls range [Ls4 = $225° - 315°$] (Fig. 11d) includes
perihelion condition (Ls = 251°, local maximum of EUV flux) as well as the peak of exospheric H density ($\sim$ Ls = 270°, see
Halekas and McFadden, 2021). It seems to contain, overall, smaller detection probabilities in the locus closest to the IMB

20

than at aphelion (Ls = 71°, local minimum of EUV flux, included in Fig. 11b). This is in agreement with the findings of
Section 3.2.3, where larger EUV flux levels create noticeably less MM-like structures in the subsolar magnetosheath than
smaller EUV levels do, as a likely result of a combination of comparatively lower plasma-$\beta$ (Rojas Mata et al., 2022) leading
to PCWs being the fastest growing mode in those conditions (Ruhunusiri et al., 2018), and, possibly, nongyrotropic effects.

From a statistical viewpoint, Fig. 11b for Ls2 (respectively, Fig. 11d for Ls4) resembles most Fig. 9a (Fig. 9b). This is in line
with the conclusions of Section 3.2.1 and Fig. 7e, where we emphasised that the Ls2 (Ls4) range is representative of low (high)
EUV flux conditions. Moreover, Ls1 and Ls3 ranges are mutually comparable as they have roughly similar PDFs over a rather
large EUV flux range: these two ranges thus mostly display changes due to seasonal effects. In this view, the Ls1 range has a
more evenly spread distribution of MM-like events around the shock, whereas the Ls3 range displays comparatively sharper
and less spatially extended features. It is interesting to note that, in contrast to other Ls ranges, the Ls4 range displays its
highest detection probability in the deep magnetospheric tail just behind the IMB (see Fig. 11d, middle plot and red region on
the rightmost plot). This is a characteristic we have seen most often displayed at high EUV fluxes (Fig. 9b) and during MY33
(Fig. 8b), which is consistent with this Ls range encompassing perihelion conditions (see Fig. 4).

## 4 Summary and conclusions

In this paper, we have aimed at creating maps of detection probabilities of MM-like structures in the Martian environment,
in a quest to better characterise mirror mode structures (MMs) across weakly magnetised and unmagnetised planets. Because
magnetometers are a common instrument on board space missions, with similar resolution and characteristics, they are an
ideal tool to compare specific low-frequency wave modes such as the ubiquitous MMs. This study is the first of two at Mars
and Venus (see Volwerk et al., 2022, for Paper II), using for the first time the same magnetic-field only detection criteria and
the same representation at both planets. At Mars, we use the MAVEN data between 2014 and 2021 and, at Venus, the Venus
Express data between 2006 and 2014.

We examined how these detection probability maps in MSO coordinates change with respect to MY, atmospheric seasons
(Ls) and solar EUV flux. Overall, MM-like structures are mostly confined to two regions, one immediately behind the bow
shock, especially at larger solar zenith angles (SZA), and one closer to the induced magnetospheric boundary (IMB). This
picture is in good agreement with previous studies at Mars (Bertucci et al., 2004; Espley et al., 2004; Simon Wedlund et al.,
2022c) and Venus (Volwerk et al., 2008, 2016; Fränz et al., 2017; Rojas Mata et al., 2022).

We linked the most dramatic changes in the spatial distribution of MM-like structures with solar EUV flux variations. First,
the regions of high MM-like occurrences contract and expand following the EUV flux-led variations of the shock and the
IMB. Second, with a similar statistics, the more EUV flux (and, to a certain extent, solar activity), the lower the probability
of detecting MM-like events around the shock and the dayside IMB. Simultaneously, high EUV flux conditions contain larger
detection probabilities in the magnetospheric tail, downstream of the IMB.

The first behaviour contradicts the simple picture that, as the solar EUV flux and ionisation levels increase in the extended
exosphere, the creation of additional pickup ions may lead to an increased ion temperature anisotropy in the entire volume of

space, both in the solar wind and in the magnetosheath – a favourable condition for MM generation. We highlight two possible reasons that may explain the discrepancy: the potential predominance of low plasma-$\beta$ at high solar activity (Rojas Mata et al., 2022), leading to an increased presence of PCWs at and around perilhelion (Romanelli et al., 2016), favouring their growth

645   over MMs, and, possibly, the nongyrotropic nature of pickup ions at Mars and Venus (Coates, 2011). Investigating in full the reason(s) of this discrepancy could be achieved by the full use of the plasma suite on board MAVEN, with the Solar Wind Ion Analyzer (SWIA) and the Solar Wind Electron Analyzer (SWEA) complementing the magnetometer data.

The second behaviour above is also reflected in changes with respect to atmospheric seasons (or solar longitude Ls): we have found that the Northern hemisphere winter season (encompassing perihelion conditions, and thus higher EUV fluxes)

650   contained less MM-like structures around the shock with compressive signatures more often observed in the magnetospheric tail (nightside downstream of the IMB). Such structures in this unusual region poses questions as to their nature, origin and characteristics and will need a dedicated study to ascertain them, preferably with the full plasma suite.

We emphasise several possible tracks to continue and expand on this first work. First, this work should be redone with coincident plasma/magnetometer measurements. Although we may lose somewhat in temporal resolution with respect to magnetic

655   field measurements (SWIA has a 8-s resolution in the magnetosheath whereas SWEA can reach down to 2 s), we will gain the certitude of a *B–N* antiphase behaviour, a necessary characteristic of MMs. Complementary techniques such as using transport ratios to characterise the low-frequency wave environment (Song et al., 1994) could also usefully be applied to the full MAVEN dataset, as shown early in the mission (Ruhunusiri et al., 2015). Comparing all of these results with our present ones will give a measure of the accuracy of the **B**-field only method over more foolproof methods and may help reinterpret past and present

660   datasets from a new perspective. Second, to expand our current study, we should also look at the dependence of MM detection probabilities with respect to upstream solar wind conditions (density, velocity, magnitude and orientation of $\mathbf{B}_{IMF}$), as well as the shock nature (quasi-parallel or quasi-perpendicular). The latter would help in determining the respective effects of unstable pickup ion distributions and quasi-perpendicular shock heating in the generation of the temperature anisotropy at the origin of MM structures. All studies could finally be performed in Mars Solar Electric coordinates, oriented along the solar wind

665   convection electric field.

*Competing interests.* No competing interests are present.

680 **References**

Ala-Lahti, M. M., Kilpua, E. K. J., Dimmock, A. P., Osmane, A., Pulkkinen, T., and Soucek, J.: Statistical analysis of mirror mode waves in sheath regions driven by interplanetary coronal mass ejection, Ann. Geophys., 36, 793–808, https://doi.org/10.5194/angeo-36-793-2018, 2018.

Allison, M. and McEwen, M.: A post-Pathfinder evaluation of areocentric solar coordinates with improved timing recipes for Mars sea-
685    sonal/diurnal climate studies, Planetary and Space Science, p. 21, 2000.

Bertucci, C., Mazelle, C., Crider, D. H., Mitchell, D. L., Sauer, K., Acuña, M. H., Connerney, J. E. P., Lin, R. P., Ness, N. F., and Winterhalter, D.: MGS MAG/ER observations at the magnetic pileup boundary of Mars: draping enhancement and low frequency waves, Advances in Space Research, 33, 1938–1944, https://doi.org/10.1016/j.asr.2003.04.054, 2004.

Brinca, A. L. and Romeiras, F. J.: On the stability of stationary nongyrotropic distribution functions: Coupling and purely growing waves, J.
690    Geophys. Res., 103, 9275–9284, https://doi.org/10.1029/97JA01995, 1998.

Coates, A.: Pickup Ion Observations at Solar System Bodies, in: Advances in Geosciences, Volume 25: Planetary Science (PS), vol. 25, pp. 11–28, https://doi.org/10.1142/9789814355377_0002, 2011.

Coates, A. J., Johnstone, A. D., and Neubauer, F. M.: Cometary ion pressure anisotropies at comets Halley and Grigg-Skjellerup, J. Geophys. Res., 101, 27 573–27 584, https://doi.org/10.1029/96JA02524, 1996.

695 Connerney, J. E. P., Espley, J., Lawton, P., Murphy, S., Odom, J., Oliversen, R., and Sheppard, D.: The MAVEN Magnetic Field Investigation, Space Sci Rev, 195, 257–291, https://doi.org/10.1007/s11214-015-0169-4, 2015.

Delva, M., Mazelle, C., and Bertucci, C.: Upstream Ion Cyclotron Waves at Venus and Mars, Space Science Reviews, 162, 5–24, https://doi.org/10.1007/s11214-011-9828-2, 2011.

Dimmock, A. P., Osmane, A., Pulkkinen, T. I., and Nykyri, K.: A statistical study of the dawn-dusk asymmetry of
700    ion temperature anisotropy and mirror mode occurrence in the terrestrial dayside magnetosheath using THEMIS data, Journal of Geophysical Research: Space Physics, 120, 5489–5503, https://doi.org/10.1002/2015JA021192, _eprint: https://onlinelibrary.wiley.com/doi/pdf/10.1002/2015JA021192, 2015.

Dong, C., Bougher, S. W., Ma, Y., Toth, G., Lee, Y., Nagy, A. F., Tenishev, V., Pawlowski, D. J., Combi, M. R., and Najib, D.: Solar wind interaction with the Martian upper atmosphere: Crustal field orientation, solar cycle, and seasonal variations, Journal of Geophysical
705    Research (Space Physics), 120, 7857–7872, https://doi.org/10.1002/2015JA020990, 2015.

Dubinin, E. and Fraenz, M.: Ultra-Low-Frequency Waves at Venus and Mars, Washington DC American Geophysical Union Geophysical Monograph Series, 216, 343–364, https://doi.org/10.1002/9781119055006.ch20, 2016.

Edberg, N. J. T., Lester, M., Cowley, S. W. H., and Eriksson, A. I.: Statistical analysis of the location of the Martian magnetic pileup boundary and bow shock and the influence of crustal magnetic fields: STATISTICAL ANALYSIS OF MPB AND BS, J. Geophys. Res., 113, n/a–n/a,
710    https://doi.org/10.1029/2008JA013096, 2008.

Edberg, N. J. T., Brain, D. A., Lester, M., Cowley, S. W. H., Modolo, R., Fränz, M., and Barabash, S.: Plasma bound-ary variability at Mars as observed by Mars Global Surveyor and Mars Express, Annales Geophysicae, 27, 3537–3550, https://doi.org/https://doi.org/10.5194/angeo-27-3537-2009, publisher: Copernicus GmbH, 2009.

Erkaev, N. V., Schaffenberger, W., Biernat, H. K., Farrugia, C. J., and Vogl, D. F.: Analysis of mirror modes convected from the bow shock
715    to the magnetopause, Planet. Space Sci., 49, 1359–1364, https://doi.org/10.1016/S0032-0633(01)00057-5, 2001.

Espley, J. R., Cloutier, P. A., Brain, D. A., Crider, D. H., and Acuña, M. H.: Observations of low-frequency magnetic oscillations in the Martian magnetosheath, magnetic pileup region, and tail, Journal of Geophysical Research: Space Physics, 109, https://doi.org/10.1029/2003JA010193, _eprint: https://onlinelibrary.wiley.com/doi/pdf/10.1029/2003JA010193, 2004.

Forbes, J. M., Lemoine, F. G., Bruinsma, S. L., Smith, M. D., and Zhang, X.: Solar flux variability of Mars' exosphere densities and temperatures, Geophysical Research Letters, 35, https://doi.org/10.1029/2007GL031904, 2008.

Fränz, M., Echer, E., Marques de Souza, A., Dubinin, E., and Zhang, T. L.: Ultra low frequency waves at Venus: Observations by the Venus Express spacecraft, Planetary and Space Science, 146, 55–65, https://doi.org/10.1016/j.pss.2017.08.011, 2017.

Garnier, P., Jacquey, C., Gendre, X., Génot, V., Mazelle, C., Fang, X., Gruesbeck, J. R., Sánchez-Cano, B., and Halekas, J. S.: The Drivers of the Martian Bow Shock Location: A Statistical Analysis of Mars Atmosphere and Volatile EvolutioN and Mars Express Observations, Journal of Geophysical Research (Space Physics), 127, e30147, https://doi.org/10.1029/2021JA030147, 2022.

Gary, S. P.: The mirror and ion cyclotron anisotropy instabilities, J. Geophys. Res., 97, 8519, https://doi.org/10.1029/92JA00299, 1992.

Gary, S. P.: Theory of Space Plasma Microinstabilities, Cambridge University Press, google-Books-ID: hMiulET5wpwC, 1993.

Gary, S. P. and Winske, D.: Correlation function ratios and the identification of space plasma instabilities, Journal of Geophysical Research: Space Physics, 97, 3103–3111, https://doi.org/10.1029/91JA02752, 1992.

Génot, V., Schwartz, S. J., Mazelle, C., Balikhin, M., Dunlop, M., and Bauer, T. M.: Kinetic study of the mirror mode, J. Geophys. Res., 106, 21 611–21 622, https://doi.org/10.1029/2000JA000457, 2001.

Génot, V., Budnik, E., Jacquey, C., Dandouras, I., and Lucek, E.: Mirror modes observed with Cluster in the Earth's magnetosheath: statistical study and IMF/solar wind dependence, in: Advances in Geosciences, vol. 14, pp. 263–283, World Scientific Publishing Company, https://doi.org/10.1142/9789812836205_0019, 2009.

Glassmeier, K. H., Motschmann, U., Mazelle, C., Neubauer, F. M., Sauer, K., Fuselier, S. A., and Acuña, M. H.: Mirror modes and fast magnetoacoustic waves near the magnetic pileup boundary of comet P/Halley, Journal of Geophysical Research: Space Physics, 98, 20 955–20 964, https://doi.org/10.1029/93JA02582, _eprint: https://onlinelibrary.wiley.com/doi/pdf/10.1029/93JA02582, 1993.

Gruesbeck, J. R., Espley, J. R., Connerney, J. E. P., DiBraccio, G. A., Soobiah, Y. I., Brain, D., Mazelle, C., Dann, J., Halekas, J., and Mitchell, D. L.: The Three-Dimensional Bow Shock of Mars as Observed by MAVEN, Journal of Geophysical Research: Space Physics, 123, 4542–4555, https://doi.org/10.1029/2018JA025366, 2018.

Halekas, J. S.: Seasonal variability of the hydrogen exosphere of Mars, Journal of Geophysical Research (Planets), 122, 901–911, https://doi.org/10.1002/2017JE005306, 2017.

Halekas, J. S. and McFadden, J. P.: Using Solar Wind Helium to Probe the Structure and Seasonal Variability of the Martian Hydrogen Corona, Journal of Geophysical Research (Planets), 126, e07049, https://doi.org/10.1029/2021JE007049, 2021.

Halekas, J. S., Taylor, E. R., Dalton, G., Johnson, G., Curtis, D. W., McFadden, J. P., Mitchell, D. L., Lin, R. P., and Jakosky, B. M.: The Solar Wind Ion Analyzer for MAVEN, Space Sci Rev, 195, 125–151, https://doi.org/10.1007/s11214-013-0029-z, 2015.

Halekas, J. S., Brain, D. A., Luhmann, J. G., DiBraccio, G. A., Ruhunusiri, S., Harada, Y., Fowler, C. M., Mitchell, D. L., Connerney, J. E. P., Espley, J. R., Mazelle, C., and Jakosky, B. M.: Flows, Fields, and Forces in the Mars-Solar Wind Interaction, Journal of Geophysical Research: Space Physics, 122, 11,320–11,341, https://doi.org/https://doi.org/10.1002/2017JA024772, _eprint: https://onlinelibrary.wiley.com/doi/pdf/10.1002/2017JA024772, 2017a.

Halekas, J. S., Ruhunusiri, S., Harada, Y., Collinson, G., Mitchell, D. L., Mazelle, C., McFadden, J. P., Connerney, J. E. P., Espley, J. R., Eparvier, F., Luhmann, J. G., and Jakosky, B. M.: Structure, dynamics, and seasonal variability of the Mars-solar wind interaction: MAVEN

Solar Wind Ion Analyzer in-flight performance and science results, Journal of Geophysical Research: Space Physics, 122, 547–578, https://doi.org/10.1002/2016JA023167, 2017b.

755    Halekas, J. S., Ruhunusiri, S., Vaisberg, O. L., Harada, Y., Espley, J., Mitchell, D. L., Mazelle, C., Romanelli, N., DiBraccio, G. A., and Brain, D. A.: Properties of Plasma Waves Observed Upstream from Mars, https://doi.org/10.1002/essoar.10503172.1, archive Location: world Library Catalog: www.essoar.org Publisher: Earth and Space Science Open Archive Section: Solar System Physics, 2020.

Hall, B. E. S., Lester, M., Sánchez-Cano, B., Nichols, J. D., Andrews, D. J., Edberg, N. J. T., Opgenoorth, H. J., Fränz, M., Holmström, M., Ramstad, R., Witasse, O., Cartacci, M., Cicchetti, A., Noschese, R., and Orosei, R.: Annual variations in the Martian
760    bow shock location as observed by the Mars Express mission, Journal of Geophysical Research: Space Physics, 121, 11,474–11,494, https://doi.org/10.1002/2016JA023316, 2016.

Hall, B. E. S., Sánchez-Cano, B., Wild, J. A., Lester, M., and Holmström, M.: The Martian Bow Shock Over Solar Cycle 23–24 as Observed by the Mars Express Mission, Journal of Geophysical Research: Space Physics, 124, 4761–4772, https://doi.org/10.1029/2018JA026404, 2019.

765    Hasegawa, A.: Drift Mirror Instability in the Magnetosphere, Phys. Fluids, 12, 2642, https://doi.org/10.1063/1.1692407, 1969.

Hoilijoki, S., Palmroth, M., Walsh, B. M., Pfau-Kempf, Y., von Alfthan, S., Ganse, U., Hannuksela, O., and Vainio, R.: Mirror modes in the Earth's magnetosheath: Results from a global hybrid-Vlasov simulation, Journal of Geophysical Research: Space Physics, 121, 4191–4204, https://doi.org/10.1002/2015JA022026, 2016.

Jarvinen, R., Kallio, E., and Pulkkinen, T. I.: Ultra-low Frequency Foreshock Waves and Ion Dynamics at Mars, Journal of Geophysical
770    Research (Space Physics), 127, e30078, https://doi.org/10.1029/2021JA030078, 2022.

Joy, S. P., Kivelson, M. G., Walker, R. J., Khurana, K. K., Russell, C. T., and Paterson, W. R.: Mirror mode structures in the Jovian magnetosheath, J. Geophys. Res., 111, A12 212, https://doi.org/10.1029/2006JA011985, 2006.

Karlsson, T., Heyner, D., Volwerk, M., Morooka, M., Plaschke, F., Goetz, C., and Hadid, L.: Magnetic Holes in the Solar Wind and Magnetosheath Near Mercury, Journal of Geophysical Research (Space Physics), 126, e28961, https://doi.org/10.1029/2020JA028961, 2021.

775    Lucek, E. A., Dunlop, M. W., Balogh, A., Cargill, P., Baumjohann, W., Georgescu, E., Haerendel, G., and Fornacon, K.-H.: Identification of magnetosheath mirror modes in Equator-S magnetic field data, Annales Geophysicae, 17, 1560–1573, https://doi.org/10.1007/s00585-999-1560-9, 1999.

Madanian, H., Halekas, J. S., Mazelle, C. X., Omidi, N., Espley, J. R., Mitchell, D. L., and McFadden, J. P.: Magnetic Holes Upstream of the Martian Bow Shock: MAVEN Observations, J. Geophys. Res. Space Physics, 125, https://doi.org/10.1029/2019JA027198, 2020.

780    Mazelle, C., Belmont, G., Glassmeier, K. H., Le Quéau, D., and Rème, H.: Ultra low frequency waves at the magnetic pile-up boundary of comet P/Halley, Advances in Space Research, 11, 73–77, https://doi.org/10.1016/0273-1177(91)90014-B, 1991.

Mazelle, C., Winterhalter, D., Sauer, K., Trotignon, J., Acuña, M., Baumgärtel, K., Bertucci, C., Brain, D., Brecht, S., Delva, M., Dubinin, E., Øieroset, M., and Slavin, J.: Bow Shock and Upstream Phenomena at Mars, Space Science Reviews, 111, 115–181, https://doi.org/10.1023/B:SPAC.0000032717.98679.d0, 2004.

785    Mitchell, D. L., Mazelle, C., Sauvaud, J.-A., Thocaven, J.-J., Rouzaud, J., Fedorov, A., Rouger, P., Toublanc, D., Taylor, E., Gordon, D., Robinson, M., Heavner, S., Turin, P., Diaz-Aguado, M., Curtis, D. W., Lin, R. P., and Jakosky, B. M.: The MAVEN Solar Wind Electron Analyzer, Space Sci Rev, 200, 495–528, https://doi.org/10.1007/s11214-015-0232-1, 2016.

Motschmann, U., Kafemann, H., and Scholer, M.: Nongyrotropy in magnetoplasmas: simulation of wave excitation and phase-space diffusion, Annales Geophysicae, 15, 603–613, https://doi.org/10.1007/s00585-997-0603-3, 1997.

790      Price, C. P.: Mirror waves driven by newborn ion distributions, J. Geophys. Res., 94, 15 001–15 009, https://doi.org/10.1029/JA094iA11p15001, 1989.

Price, C. P., Swift, D. W., and Lee, L.-C.: Numerical simulation of nonoscillatory mirror waves at the Earth's magnetosheath, Journal of Geophysical Research: Space Physics, 91, 101–112, https://doi.org/10.1029/JA091iA01p00101, 1986.

Rojas Mata, S., Stenberg Wieser, G., Futaana, Y., Bader, A., Persson, M., Fedorov, A., and Zhang, T.: Proton Temperature Anisotropies in
795      the Venus Plasma Environment During Solar Minimum and Maximum, Journal of Geophysical Research (Space Physics), 127, e29611, https://doi.org/10.1029/2021JA029611, 2022.

Romanelli, N., Bertucci, C., Gómez, D., Mazelle, C., and Delva, M.: Proton cyclotron waves upstream from Mars: Observations from Mars Global Surveyor, Planet. Space Sci., 76, 1–9, https://doi.org/10.1016/j.pss.2012.10.011, 2013.

Romanelli, N., Mazelle, C., Chaufray, J. Y., Meziane, K., Shan, L., Ruhunusiri, S., Connerney, J. E. P., Espley, J. R., Eparvier, F., Thiemann,
800      E., Halekas, J. S., Mitchell, D. L., McFadden, J. P., Brain, D., and Jakosky, B. M.: Proton cyclotron waves occurrence rate upstream from Mars observed by MAVEN: Associated variability of the Martian upper atmosphere, Journal of Geophysical Research (Space Physics), 121, 11,113–11,128, https://doi.org/10.1002/2016JA023270, 2016.

Romeo, O. M., Romanelli, N., Espley, J. R., Mazelle, C., DiBraccio, G. A., Gruesbeck, J. R., and Halekas, J. S.: Variability of Upstream Proton Cyclotron Wave Properties and Occurrence at Mars Observed by MAVEN, Journal of Geophysical Research (Space Physics), 126,
805      e28616, https://doi.org/10.1029/2020JA028616, 2021.

Ruhunusiri, S., Halekas, J. S., Connerney, J. E. P., Espley, J. R., McFadden, J. P., Larson, D. E., Mitchell, D. L., Mazelle, C., and Jakosky, B. M.: Low-frequency waves in the Martian magnetosphere and their response to upstream solar wind driving conditions, Geophysical Research Letters, 42, 8917–8924, https://doi.org/10.1002/2015GL064968, 2015.

Ruhunusiri, S., Halekas, J. S., Espley, J. R., Eparvier, F., Brain, D., Mazelle, C., Harada, Y., DiBraccio, G. A., Thiemann, E. M. B., Larson,
810      D. E., Mitchell, D. L., Jakosky, B. M., and Sulaiman, A. H.: One-Hertz Waves at Mars: MAVEN Observations, Journal of Geophysical Research (Space Physics), 123, 3460–3476, https://doi.org/10.1029/2017JA024618, 2018.

Schwartz, S. J., Burgess, D., and Moses, J. J.: Low-frequency waves in the Earth's magnetosheath: present status, Annales Geophysicae, 14, 1134–1150, https://doi.org/10.1007/s00585-996-1134-z, 1997.

Simon Wedlund, C., Volwerk, M., Beth, A., Mazelle, C., Möstl, C., Halekas, J., Gruesbeck, J., and Rojas-Castillo, D.: Predicted times of
815      bow Shock crossings at Mars from the NASA/MAVEN mission, using spacecraft ephemerides and magnetic field data, with a predictor-corrector algorithm, https://doi.org/10.5281/zenodo.5725288, dataset, 2022a.

Simon Wedlund, C., Volwerk, M., Beth, A., Mazelle, C., Möstl, C., Halekas, J., Gruesbeck, J. R., and Rojas-Castillo, D.: A Fast Bow Shock Location Predictor-Estimator From 2D and 3D Analytical Models: Application to Mars and the MAVEN Mission, Journal of Geophysical Research: Space Physics, 127, e2021JA029 942, https://doi.org/https://doi.org/10.1029/2021JA029942, e2021JA029942 2021JA029942,
820      2022b.

Simon Wedlund, C., Volwerk, M., Mazelle, C., Halekas, J., Rojas-Castillo, D., Espley, J., and Möstl, C.: Making Waves: Mirror Mode Structures Around Mars Observed by the MAVEN Spacecraft, Journal of Geophysical Research: Space Physics, 127, e2021JA029 811, https://doi.org/https://doi.org/10.1029/2021JA029811, e2021JA029811 2021JA029811, 2022c.

Song, P., Russell, C. T., and Gary, S. P.: Identification of low-frequency fluctuations in the terrestrial magnetosheath, J. Geophys. Res., 99,
825      6011, https://doi.org/10.1029/93JA03300, 1994.

Sonnerup, B. U. Ö. and Scheible, M.: Minimum and Maximum Variance Analysis, in: Analysis Methods for Multi-Spacecraft Data, no. SR-001 in ISSI Scientific Report, pp. 185–220, ISSI/ESA, götz paschmann and patrick w. daly edn., 1998.

Soucek, J., Lucek, E., and Dandouras, I.: Properties of magnetosheath mirror modes observed by Cluster and their response to changes in plasma parameters, Journal of Geophysical Research: Space Physics, 113, https://doi.org/10.1029/2007JA012649, 2008.

830 Szegö, K., Glassmeier, K.-H., Bingham, R., Bogdanov, A., Fischer, C., Haerendel, G., Brinca, A., Cravens, T., Dubinin, E., Sauer, K., Fisk, L., Gombosi, T., Schwadron, N., Isenberg, P., Lee, M., Mazelle, C., Möbius, E., Motschmann, U., Shapiro, V. D., Tsurutani, B., and Zank, G.: Physics of Mass Loaded Plasmas, Space Sci. Rev., 94, 429–671, https://doi.org/10.1023/A:1026568530975, 2000.

Thiemann, E. M. B., Chamberlin, P. C., Eparvier, F. G., Templeman, B., Woods, T. N., Bougher, S. W., and Jakosky, B. M.: The MAVEN EUVM model of solar spectral irradiance variability at Mars: Algorithms and results, Jour-

835 nal of Geophysical Research: Space Physics, 122, 2748–2767, https://doi.org/https://doi.org/10.1002/2016JA023512, _eprint: https://onlinelibrary.wiley.com/doi/pdf/10.1002/2016JA023512, 2017.

Trainer, M. G., Wong, M. H., McConnochie, T. H., Franz, H. B., Atreya, S. K., Conrad, P. G., Lefèvre, F., Mahaffy, P. R., Malespin, C. A., Manning, H. L. K., Martín-Torres, J., Martínez, G. M., McKay, C. P., Navarro-González, R., Vicente-Retortillo, Á., Webster, C. R., and Zorzano, M.-P.: Seasonal Variations in Atmospheric Composition as Measured in Gale Crater,

840 Mars, Journal of Geophysical Research: Planets, 124, 3000–3024, https://doi.org/https://doi.org/10.1029/2019JE006175, _eprint: https://onlinelibrary.wiley.com/doi/pdf/10.1029/2019JE006175, 2019.

Treumann, R. A., Jaroschek, C. H., Constantinescu, O. D., Nakamura, R., Pokhotelov, O. A., and Georgescu, E.: The strange physics of low frequency mirror mode turbulence in the high temperature plasma of the magnetosheath, Nonlin. Processes Geophys., 11, 647–657, https://doi.org/10.5194/npg-11-647-2004, 2004.

845 Trotignon, J., Mazelle, C., Bertucci, C., and Acuña, M.: Martian shock and magnetic pile-up boundary positions and shapes determined from the Phobos 2 and Mars Global Surveyor data sets, Planetary and Space Science, 54, 357–369, https://doi.org/10.1016/j.pss.2006.01.003, 2006.

Tsurutani, B. T., Lakhina, G. S., Verkhoglyadova, O. P., Echer, E., Guarnieri, F. L., Narita, Y., and Constantinescu, D. O.: Magnetosheath and heliosheath mirror mode structures, interplanetary magnetic decreases, and linear magnetic decreases: Differences and distinguishing

850 features: REVIEW, J. Geophys. Res., 116, n/a–n/a, https://doi.org/10.1029/2010JA015913, 2011.

Turner, J. M., Burlaga, L. F., Ness, N. F., and Lemaire, J. F.: Magnetic holes in the solar wind, J. Geophys. Res., 82, 1921, https://doi.org/10.1029/JA082i013p01921, 1977.

Volwerk, M., Zhang, T. L., Delva, M., Vörös, Z., Baumjohann, W., and Glassmeier, K.-H.: Mirror-mode-like structures in Venus' induced magnetosphere, J. Geophys. Res., 113, E00B16, https://doi.org/10.1029/2008JE003154, 2008.

855 Volwerk, M., Schmid, D., Tsurutani, B. T., Delva, M., Plaschke, F., Narita, Y., Zhang, T., and Glassmeier, K.-H.: Mirror mode waves in Venus's magnetosheath: solar minimum vs. solar maximum, Ann. Geophys., 34, 1099–1108, https://doi.org/10.5194/angeo-34-1099-2016, 2016.

Volwerk, M., Mautner, D., Wedlund, C. S., Goetz, C., Plaschke, F., Karlsson, T., Schmid, D., Rojas-Castillo, D., Roberts, O. W., and Varsani, A.: Statistical study of linear magnetic hole structures near Earth, Ann. Geophys., 39, 239–253, https://doi.org/10.5194/angeo-39-239-

860 2021, 2021.

Volwerk, M., Simon Wedlund, C., Mautner, C., Stenberg Wieser, G., Rojas Mata, S., Futaana, Y., Mazelle, M., Rojas-Castillo, D., Bertucci, C., and Delva, M.: Statistical distribution of mirror mode-like structures in the magnetosheaths of unmagnetised planets: 2. Venus as observed by the Venus Express spacecraft, Annales Geophysicae, submitted, 1–15, 2022.

Wilson III, L. B., Stevens, M. L., Kasper, J. C., Klein, K. G., Maruca, B. A., Bale, S. D., Bowen, T. A., Pulupa, M. P., and Salem, C. S.:

865      The Statistical Properties of Solar Wind Temperature Parameters Near 1 au, ApJS, 236, 41, https://doi.org/10.3847/1538-4365/aab71c,

publisher: American Astronomical Society, 2018.

Yamauchi, M., Hara, T., Lundin, R., Dubinin, E., Fedorov, A., Sauvaud, J. A., Frahm, R. A., Ramstad, R., Futaana, Y., Holmstrom, M., and

Barabash, S.: Seasonal variation of Martian pick-up ions: Evidence of breathing exosphere, Planetary and Space Science, 119, 54–61,

https://doi.org/10.1016/j.pss.2015.09.013, 2015.
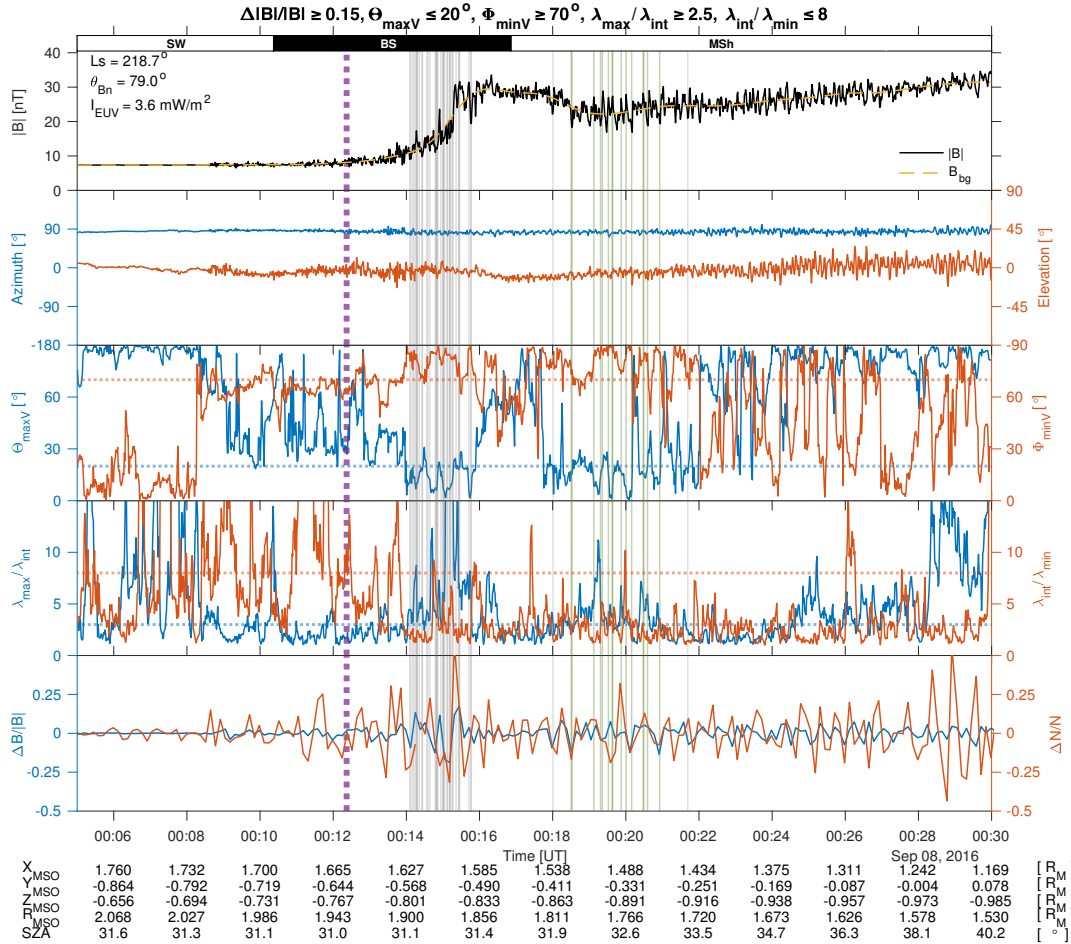
**Figure 1.** Example of MM-like detections at Mars, using the $B$-field-only criteria of Table 1 on 8 Sept. 2016, at relatively high solar activity. From top to bottom: Total magnetic field strength, with $B_{bg}$ the background magnetic field calculated as a Butterworth low-pass filter over 2 min; Magnetic field azimuth (left axis) and elevation (right axis) angles; MVA angles between the maximum (minimum) variance eigenvector direction $\Theta_{maxV}$ and that of the background **B**-field on left axis ($\Phi_{minV}$ on right axis). The threshold values for selections of MMs are indicated in blue and red dotted lines, for each respective angle; MVA eigenvalue ratios $\lambda_{max}/\lambda_{int}$ on left axis ($\lambda_{int}/\lambda_{min}$, right axis), with their respective thresholds in dotted lines; Magnetic field and ion density variations so that $\Delta B/B = \left(|\mathbf{B}| - B_{bg}\right)/B_{bg}$ and $\Delta N/N = \left(N - N_{bg}\right)/N_{bg}$ need to be in antiphase with respect to 0 for a typical MM behaviour. We downsample the magnetic field variations to the resolution of that of the ion instrument and calculate the background density $N_{bg}$ using the same Butterworth filter as for **B**. In the solar wind before 00:15 UT, the SWIFA mode (4 s resolution) of SWIA is chosen for the calculation of the density moment variation, whereas afterwards the SWICA mode is preferred (8 s resolution) as per the recommendation of Halekas et al. (2017b). We indicate below the figure $X_{MSO}$, $Y_{MSO}$, $Z_{MSO}$, radial distance $R_{MSO}$ in units of Mars' radius $R_M$, as well as solar zenith angle SZA $= \arctan\sqrt{Y^2_{MSO} + Z^2_{MSO}}/X_{MSO}$. Solar longitude was Ls $\approx 220°$ and average solar EUV flux $\langle I_{EUV}\rangle \approx 3.6\,\mathrm{mW\,m^{-2}}$. The angle $\theta_{Bn}$ between the bow shock normal and the interplanetary magnetic field direction was determined to be $\theta_{Bn} \approx 80°$ (reminiscent of quasi-perpendicular bow shock conditions) assuming a smooth shock geometry as explained in Simon Wedlund et al. (2022b). The original detections using Criteria 1–4 of Table 1 appear as grey and green vertical lines, with the green portion representing the final detections with removal of false positives (Criteria 1–4 and 5–6, and Sect. 2.2.2). The start position of the bow shock region in dotted purple is estimated through the predictor-corrector algorithm of Simon Wedlund et al. (2022b). To replace this event in MAVEN's timeline of EUV activity and Ls ranges, see first orange dot on Fig. 4.
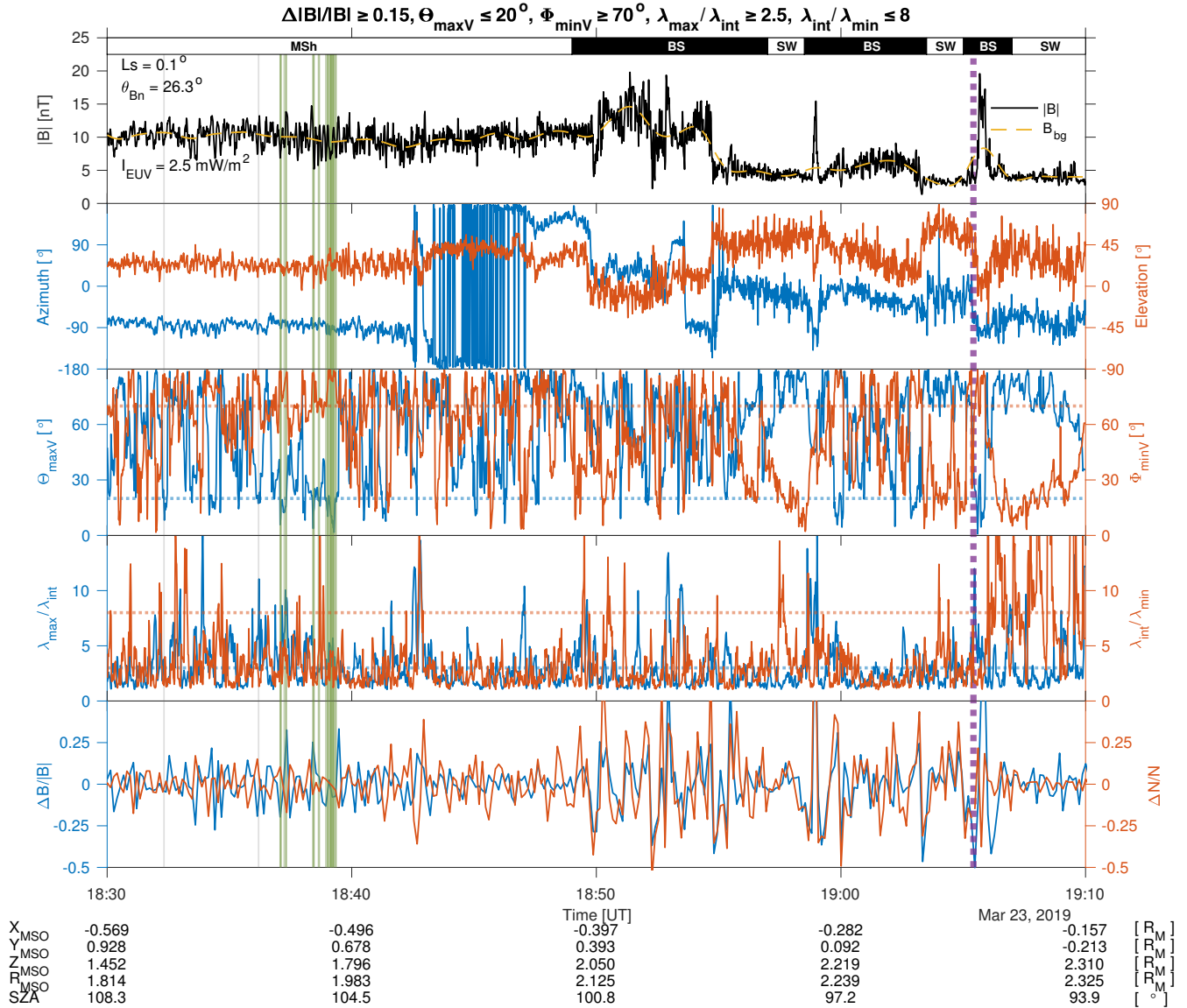
**Figure 2.** Example of MM-like detections at Mars, using the *B*-field-only criteria of Table 1 on 23 Mar. 2019, at relatively low solar activity. Conditions were: Ls ≈ 220°, $\langle I_{EUV} \rangle \approx 2.5\ \mathrm{mW\,m^{-2}}$ and $\theta_{Bn} \approx 25°$ (reminiscent of quasi-parallel bow shock conditions). Ion density moments were calculated with the 8-s SWICA mode in the magnetosheath before 18:54 UT, and with the 4-s SWIFA mode afterwards. Otherwise, same caption as in Fig. 1. To replace this event in MAVEN's timeline of EUV activity and Ls ranges, see second orange dot on Fig. 4.
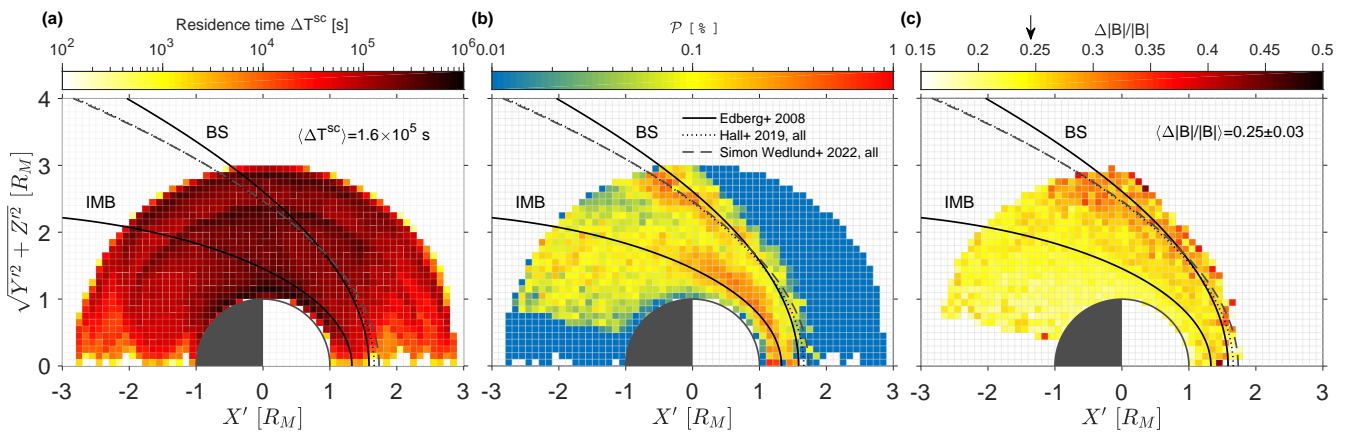
**Figure 3.** Mission-wide results at Mars as observed by the MAVEN/MAG instrument from MY32 to MY35 (1 Nov. 2014 to 7 Feb. 2021). (a) Spacecraft residence time $\Delta T^{\mathrm{sc}}$. (b) Percentage occurrence of detecting MM-like structures $\mathcal{P}$. (c) Magnetic field fluctuations $\Delta|\mathbf{B}|/B_{\mathrm{bg}}$. On panel (c), the mean magnetic fluctuation of $0.25 \pm 0.03$ is highlighted by an arrow on the colour bar. In panel (a), the average residence time in a grid cell $0.1 \times 0.1 R_M$, noted $\langle \Delta T^{\mathrm{sc}} \rangle$ is given for reference. The average positions of the bow shock (BS) and of the induced magnetospheric boundary (IMB) are given for reference as black continuous lines (Edberg et al., 2008), in dotted lines (Hall et al., 2019, all points) and as dashed lines (Simon Wedlund et al., 2022b, all points). They roughly delimit the magnetosheath region, although detections outside of the average bow shock are always inside the shock for individual events. Coordinates are solar wind-aberrated, normalised to the radius of Mars ($R_M = 3389.5$ km).
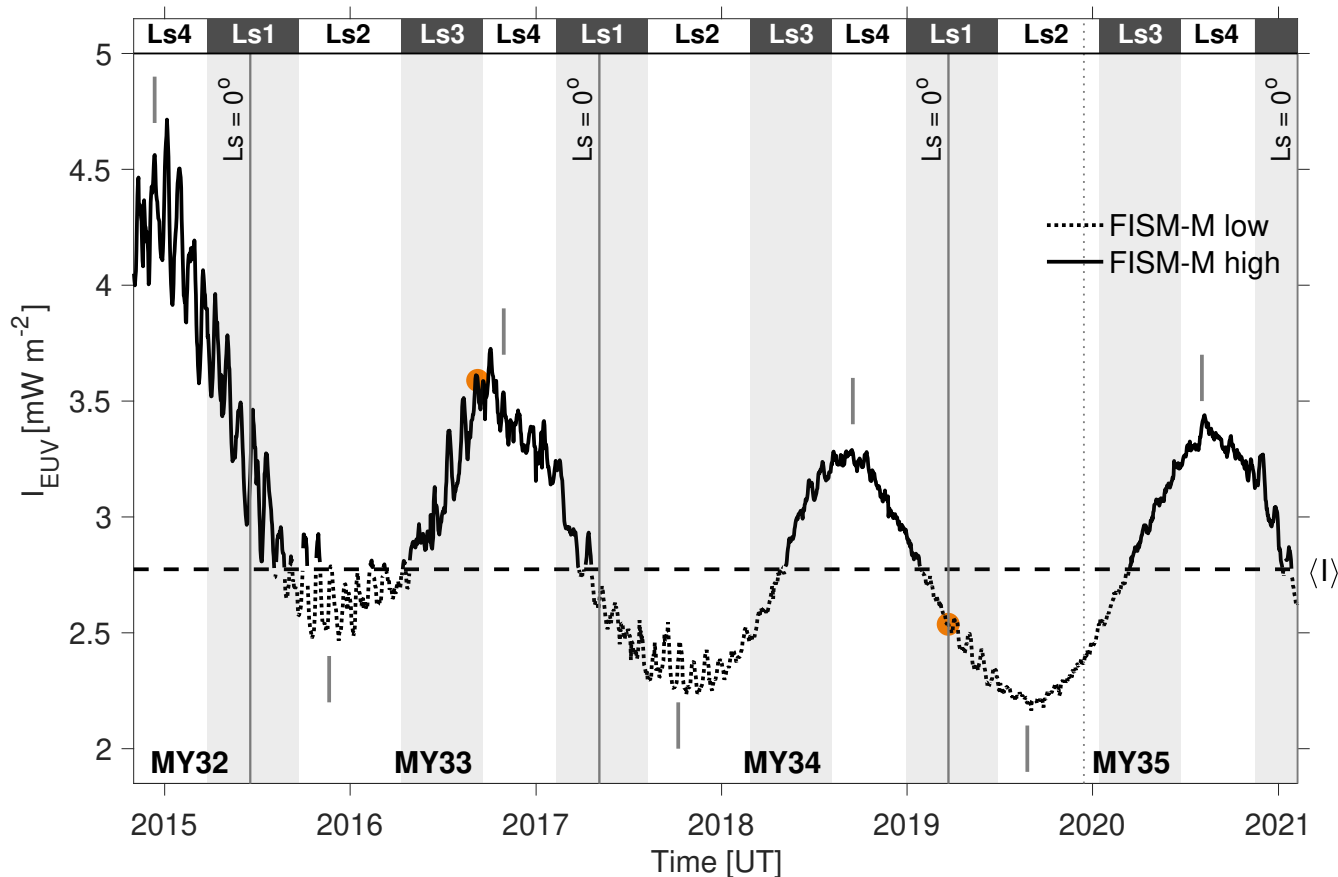
**Figure 4.** Lyman-$\alpha$ daily modelled irradiance levels $I_{\mathrm{EUV}}$ between MY32 and MY35 as derived from the EUVM instrument on board MAVEN and corrected with the FISM-M EUVM model (Thiemann et al., 2017). The median of the irradiance throughout this period $\langle I \rangle$ is 2.77 mW m$^{-2}$ (horizontal dashed line) which separates in our study high EUV conditions from low EUV conditions at Mars. Mars years (MYs) and northern hemisphere seasons (Ls) are highlighted, with Ls = 0° marking the northern spring equinox and the start of a new Mars Year. Here, Ls1 = [315°–45°], Ls2 = [45°–135°], Ls3 = [135°–225°] and Ls4 = [225°–315°] for brevity. The timings of aphelia (local minima of $I_{\mathrm{EUV}}$, Ls = 71°) and perihelia (local maxima, Ls = 251°) are indicated as short vertical grey lines. Solar cycle 25 started in December 2019, marked as a vertical dotted line. The orange dots correspond to the timings of the two examples presented in Figs. 1 and 2.
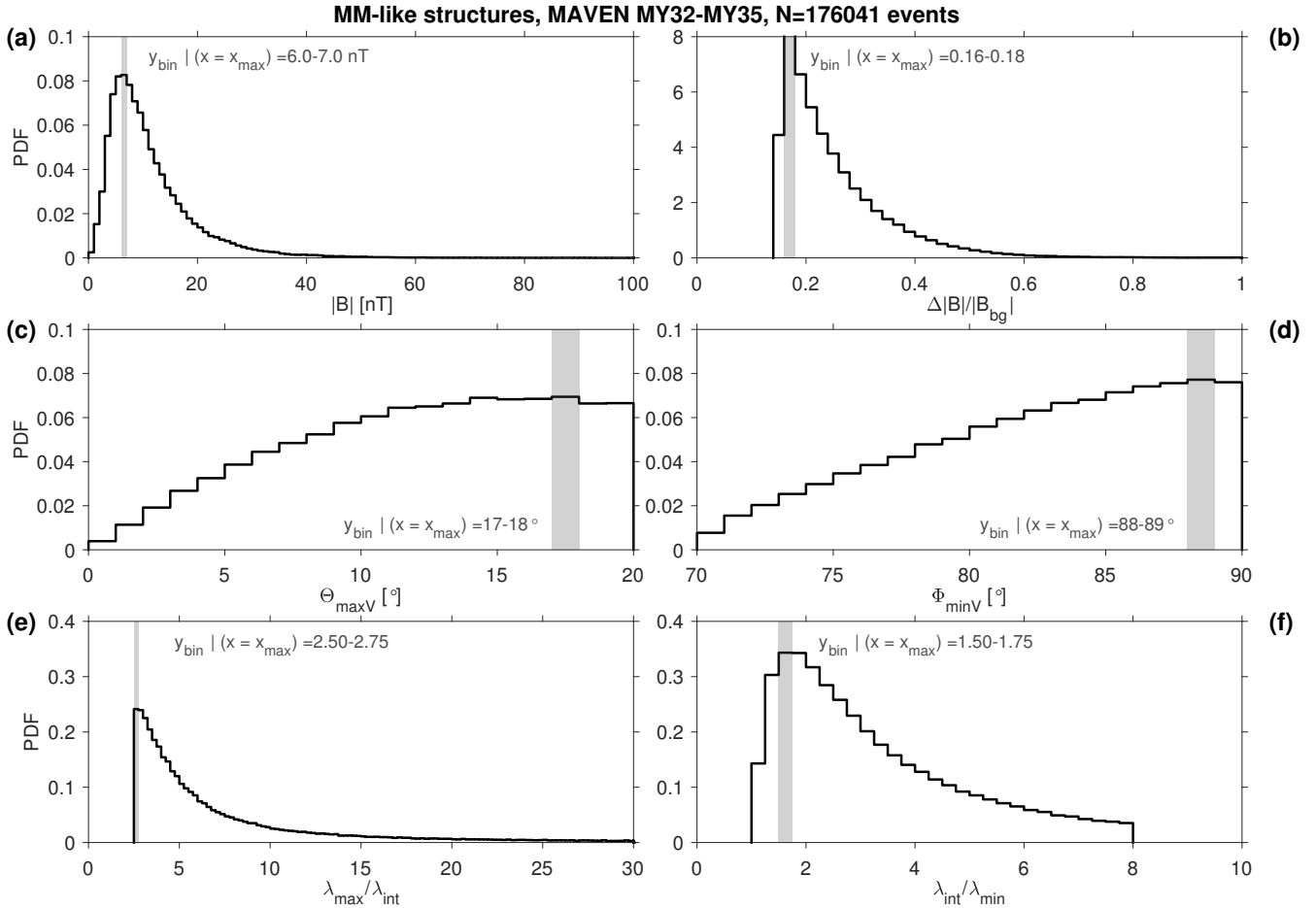
**Figure 5.** Probability density functions (PDF) for the criteria given in Table 1 for the MM-like structures detected with MAVEN/MAG from MY32 to MY35 (1 November 2014 to 7 February 2021). (a): Total magnetic field intensity $|\mathbf{B}|$, in bins of 1 nT. (b) Magnetic field fluctuations $\Delta|\mathbf{B}|/B_{\rm bg}$, in bins of 0.02. (c) and (d): Angles between average magnetic field direction and maximum (minimum) variance direction $\Theta_{\rm maxV}$ ($\Phi_{\rm minV}$), in bins of 1°. (e) and (f): Ratios of maximum to intermediate $\lambda_{\rm max}/\lambda_{\rm int}$ (intermediate to minimum, $\lambda_{\rm int}/\lambda_{\rm min}$) eigenvalues, in bins of 0.25. The position of the maximum of the PDF and its typical bin is marked by a grey zone. All bins are uniformly distributed.
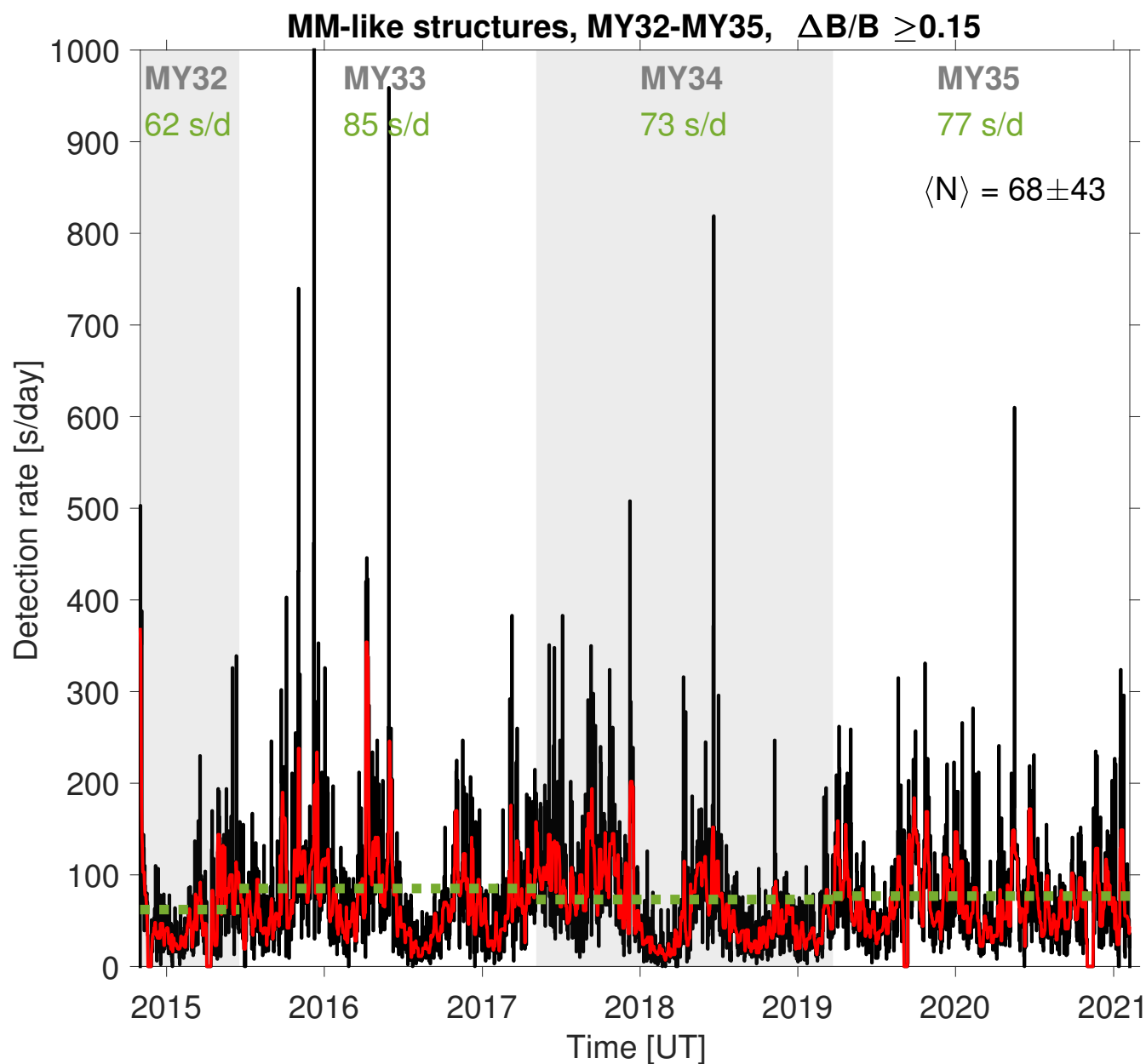
**Figure 6.** Daily detection rate of MM-like structures as observed by the MAVEN/MAG instrument from MY32 to MY35 (1 November 2014 to 7 February 2021), using the criteria of Table 1. The red line corresponds to the running mean of the black curve over 7 days, and the green dotted line corresponds to Mars Year averages (given as numbers in the top). $\langle N \rangle$ is the median of the whole signal in black, with its corresponding standard deviation.
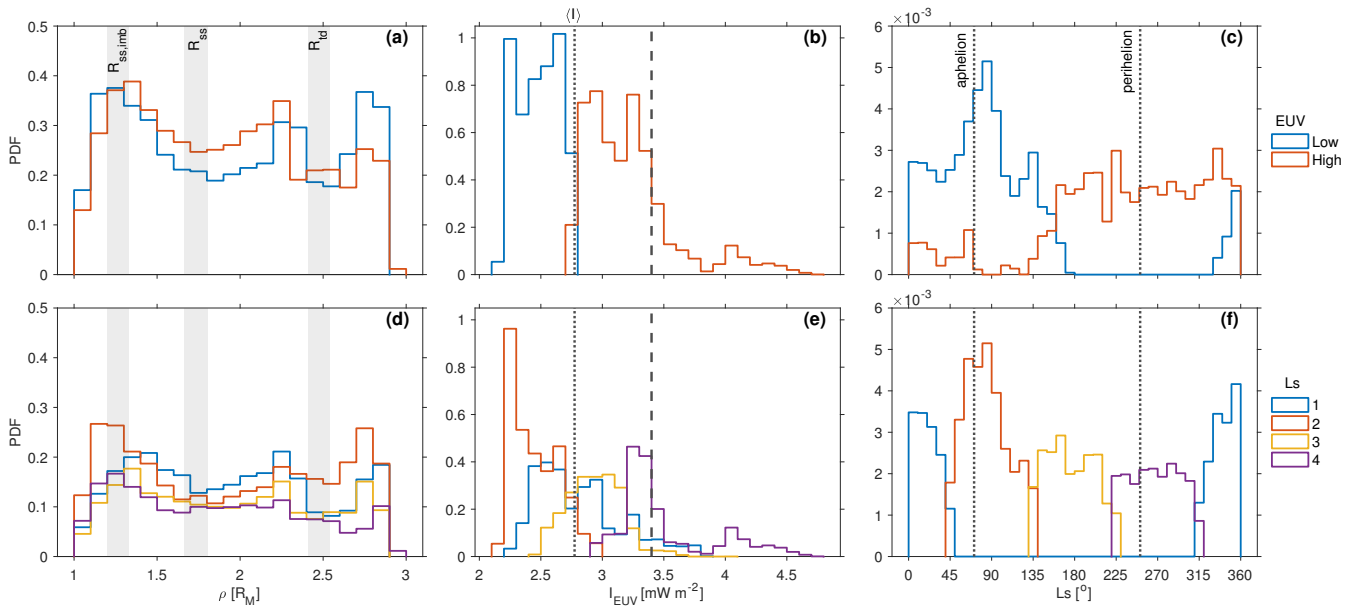
**Figure 7.** Probability Density Functions (PDF) of $176{,}041$ MM-like structures detected from the end of MY32 to the end of MY35. Panels (a-c) discriminate between two irradiance levels, $I_{EUV} < 2.77\,\mathrm{mW\,m^{-2}}$ (low EUV flux, blue lines) and $I_{EUV} \geq 2.77\,\mathrm{mW\,m^{-2}}$ (high EUV flux, red lines). Panels (d-f) discriminate between four Ls seasons (Ls1–4), as defined in Fig. 4. These PDFs are calculated for the following parameters: Panels (a) and (d): Radial polar coordinate $\rho = \sqrt{X'^2 + Y'^2 + Z'^2}$, in bins of $0.1\,R_M$. The radius of Mars is $R_M = 3389.5\,\mathrm{km}$; Panels (b) and (e): EUV irradiance $I_{EUV}$, in bins of $0.1\,\mathrm{mW\,m^{-2}}$; Panels (c) and (f): Seasons (Ls), in bins of $10°$. The PDF is normalised to the the total number of detected events, i.e., $176{,}041$. Some remarkable features are pointed out by a vertical dashed line, i.e., transition region in PDF on panels (b) and (e). Moreover, we also include: in panels (a) and (d), the range of positions of the subsolar and terminator standoff bow shock distances $R_{ss}$ and $R_{td}$ (Simon Wedlund et al., 2022b, between low and high EUV conditions) and the range of subsolar IMB positions, $R_{ss,imb}$ (Trotignon et al., 2006; Edberg et al., 2008); In panels (b) and (e), the median value of the EUV flux $\langle I \rangle$; In panels (c) and (f), the aphelion (Ls = 71°) and perihelion positions (Ls = 251°).
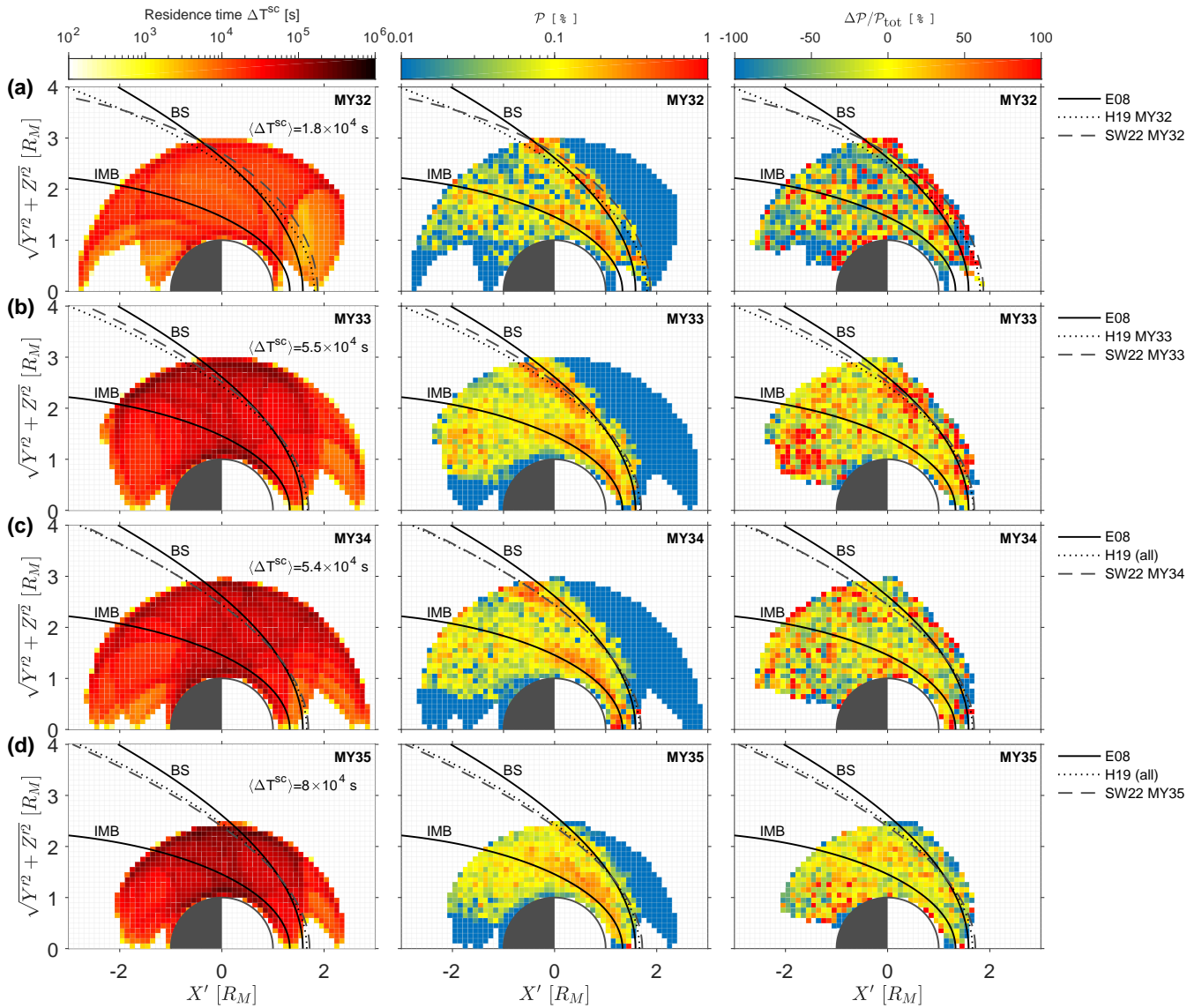
**Figure 8.** Residence time (left), probability $\mathcal{P}$ of detecting MM-like structures (middle) and departure from the total detection probability $\Delta\mathcal{P}/\mathcal{P}_{\text{tot}}$ (right) at Mars, binned by MY. The percentage difference is calculated as $\Delta\mathcal{P}/\mathcal{P} = \left(\mathcal{P}_{\text{MY}} - \mathcal{P}_{\text{tot}}\right)/\mathcal{P}_{\text{tot}}$, with positive hot-hued (negative cold-hued) values showing where $\mathcal{P}_{\text{MY}} > \mathcal{P}_{\text{tot}}$ ($\mathcal{P}_{\text{MY}} < \mathcal{P}_{\text{tot}}$). The total rate $\mathcal{P}_{\text{tot}}$ is taken from Fig. 3b. $B$-field data only with MAVEN/MAG were used in the detection, from 1 November 2014 to 7 February 2021. (a) MY32. (b) MY33. (c) MY34. (d) MY35. Bow shock average positions are shown as dotted lines (Hall et al., 2019, MY32, MY33 and all points) and as dashed lines (Simon Wedlund et al., 2022b, for each MY). See also caption of Fig. 3 for other details.
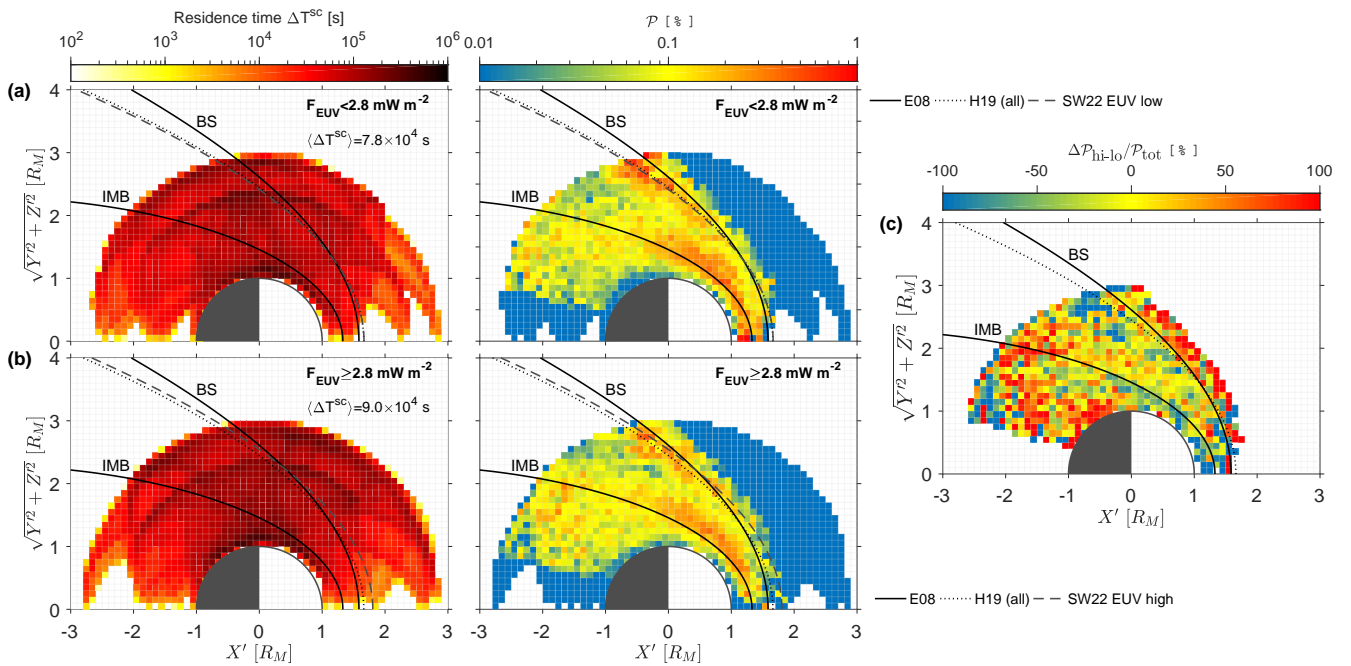
**Figure 9.** Residence time (left) and probability $\mathcal{P}$ in % of detecting MM-like structures (middle) at Mars, with respect to EUV irradiance levels. (a) Low EUV fluxes. (b) High EUV fluxes. (c) Relative difference between high and low EUV levels with respect to the total detection probability, $\Delta\mathcal{P}_{\text{hi-lo}}/\mathcal{P}_{\text{tot}} = (\mathcal{P}_{\text{hi}} - \mathcal{P}_{\text{lo}})/\mathcal{P}_{\text{tot}}$, expressed in percentage. As before, $\mathcal{P}_{\text{tot}}$ is the map obtained in Fig. 3b. The colour yellow indicates regions with the same probabilities between the two conditions, whereas blue-green 'cold' hue (orange-red, 'hot' hue) regions indicate where $\mathcal{P}$ is dominated by low (high) EUV conditions. Bow shock average positions are shown as dotted lines (Hall et al., 2019, all points) and as dashed lines (Simon Wedlund et al., 2022b, for each EUV flux level). See also caption of Fig. 3 for other details.
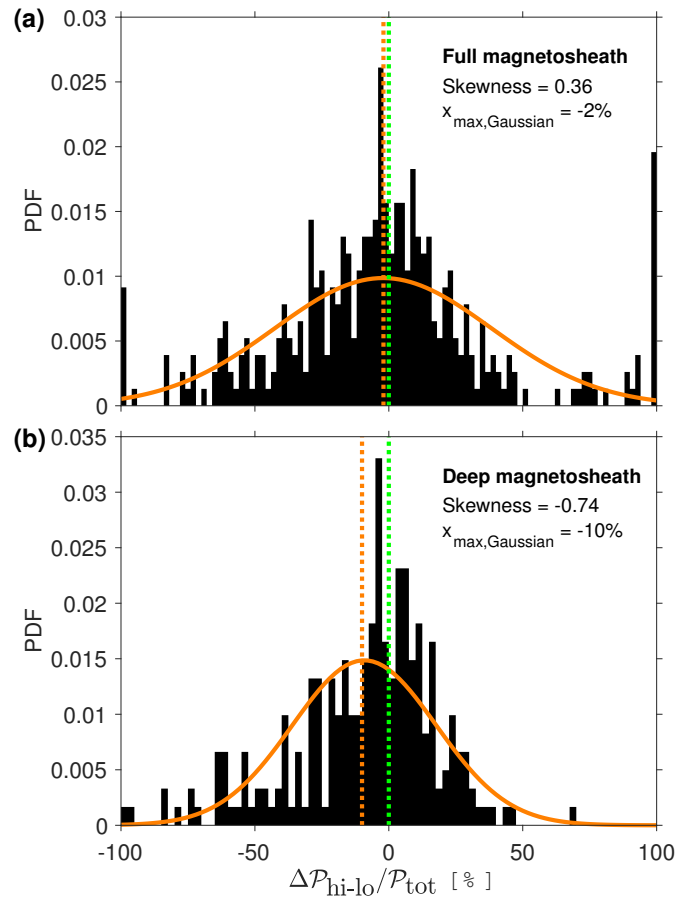
**Figure 10.** Probability Density Function of EUV-discriminated relative detection probabilities, for the 'full magnetosheath' (a), and for the 'deep magnetosheath' (b). As in Fig. 9c, we calculate the relative difference between high and low EUV levels with respect to the total detection probability, $\Delta\mathcal{P}_{\text{hi-lo}}/\mathcal{P}_{\text{tot}} = (\mathcal{P}_{\text{hi}} - \mathcal{P}_{\text{lo}})/\mathcal{P}_{\text{tot}}$, expressed in percentage, with positive values showing preponderance towards high EUV conditions, and negative values towards low EUV conditions. 'Full magnetosheath' considers the detection probabilities outside of the average IMB (defined by the fit of Edberg et al., 2008), whereas 'Deep magnetosheath' only considers $\mathcal{P}$ in the narrow region delimited by the two black continuous lines in Fig. 9c, between the two average fits of Edberg et al. (2008). Gaussian fits to the distributions are shown in orange, together with their peak position (dashed vertical line). The symmetric position where $\mathcal{P}_{\text{hi}} = \mathcal{P}_{\text{lo}}$ is given as green vertical line. Deviation from the Gaussian fit (in orange) is given by the skewness of the distributions: negative skewness highlights a distribution whose mass is concentrated on the left (low EUV conditions), whereas a positive skewness has the distribution concentrated towards the right (high EUV conditions).
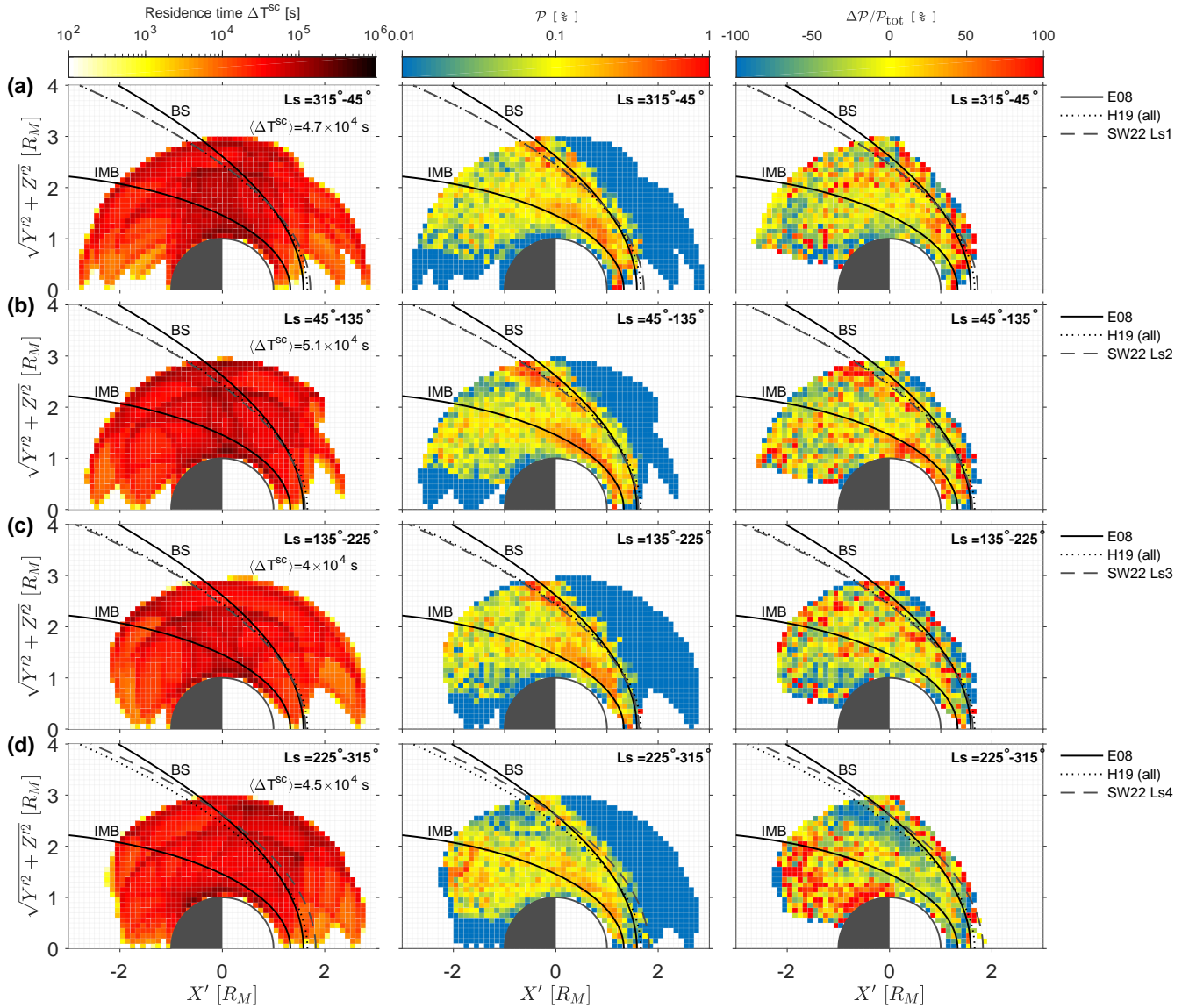
**Figure 11.** Residence time (left) and probability $\mathcal{P}$ of detecting MM-like structures (middle) at Mars, and departure from total detection probability $\Delta\mathcal{P}/\mathcal{P}_{\text{tot}}$ (right), with respect to Mars season (binned by Ls). (a) Ls = $[315° - 45°]$ = Ls1. (b) Ls = $[45° - 135°]$ = Ls2. (c) Ls = $[135° - 225°]$ = Ls3. (d) Ls = $[225° - 315°]$ = Ls4. The percentage difference is calculated as $\Delta\mathcal{P}/\mathcal{P} = (\mathcal{P}_{\text{Ls}} - \mathcal{P}_{\text{tot}})/\mathcal{P}_{\text{tot}}$, with positive hot-hued (negative cold-hued) values showing where $\mathcal{P}_{\text{Ls}} > \mathcal{P}_{\text{tot}}$ ($\mathcal{P}_{\text{Ls}} < \mathcal{P}_{\text{tot}}$). The total rate $\mathcal{P}_{\text{tot}}$ is taken from Fig. 3b. Bow shock average positions are shown as dotted lines (Hall et al., 2019, all points) and as dashed lines (Simon Wedlund et al., 2022b, for each Ls range). See also caption of Fig. 3 for other details.